Available online at www.keaipublishing.com/en/journals/journal-of-magnesium-and-alloys/

ScienceDirect

Journal of Magnesium and Alloys 13 (2025) 486–509

www.elsevier.com/locate/jma

Review

An overview of the recent developments in biodegradable Mg-Zn alloy

Manas Ranjan Sahu*, Akiko Yamamoto

Research Centre for Macromolecules and Biomaterials, National Institute for Materials Science, 1-1 Namiki, Tsukuba, Ibaraki 305-0044, Japan

Received 8 December 2024; received in revised form 10 January 2025; accepted 14 January 2025
Available online 3 February 2025

Abstract

The increasing interest in Mg-Zn binary alloys as temporary implant materials is attributed to their outstanding biocompatibility, biodegradability, and favourable mechanical properties. However, their application is constrained by high degradation rates in the physiological environment, resulting in the release of hydrogen gas and a rapid decline in mechanical properties. Additionally, the material's biocompatibility is contingent upon its degradability. Researchers have demonstrated that addressing these issues is possible through strategies such as controlling Zn content, employing thermo-mechanical processing to achieve suitable microstructures, and applying surface coatings. This manuscript provides a comprehensive review of published literature on Mg-Zn alloys, exploring the challenges and outlining future research directions in this field.

Keywords: Mg-Zn alloy; Degradation; Temporary implant; Biocompatibility.

1. Introduction

Biodegradable metals represent a class of metals designed to be corroded gradually *in vivo*, with an appropriate host response elicited by released corrosion products, which can pass through, be metabolized, or assimilated by cells and tissue. Then, they dissolve completely upon fulfilling the mission to assist tissue healing with no implant residues [1]. Unlike traditional permanent implant materials such as titanium, stainless steel, and cobalt-chromium alloys, biodegradable metals offer a solution for temporary implants to their common complications like stress shielding, bone thickening, implant loosening, and chronic inflammation, together with the elimination of secondary removal surgery after tissue healing [2,3]. The representative temporary implants are cardiovascular stents and fracture fixation devices such as bone plates and screws. These devices have been commercialized with permanent metallic materials such as a Co-Cr alloy for cardiovascular stents and Ti (grade 2) for microplates and screws, followed by the products employing bioabsorbable polymers such as poly-L-lactic acids. Table 1 presents the mechanical properties of typical implant materials with bone tissue.

Among all the available metallic elements in the periodic table, the metals or alloys having basic characteristics such as complete biodegradability and biocompatibility for each alloying element with good mechanical properties, are the most promising candidates to be considered as biodegradable metals [1]. For biodegradability, the metals and/or alloys with a standard electrode potential lower than that of hydrogen ($E^0 = 0$ V) are considered to be corroded in the physiological environment by reacting with water in body fluids. For biocompatibility, the composition of existing elements in the human body and their threshold concentrations in a healthy tissue provide a valuable reference for selecting the composition of biodegradable metals for clinical implant use. For mechanical properties, the biodegradable metals should provide sufficient support (varies as per the implantation site) immediately after the post implantation until tissue starts to heal.

In this context, magnesium (Mg), iron (Fe), zinc (Zn), and their alloys are the candidates most commonly considered as biodegradable metals for temporary implant applications. Fe and its alloys possess outstanding mechanical properties and

---

* Corresponding author.
E-mail address: SAHU.MANASRANJAN@nims.go.jp (M.R. Sahu).

https://doi.org/10.1016/j.jma.2025.01.011

Table 1
The mechanical properties of implant materials with bone tissue.

Material	Young's modulus (GPa)	Yield strength (MPa)	Compression strength (MPa)	Tensile strength (MPa)	Fracture toughness ($MPa.m^{½}$)	Ref
Cortical bone	7 – 30	–	100 – 230	164 – 240	2 – 12	[23,24]
Stainless steel 316L	193	170 – 310	480 – 620	540 – 1000	~100	[23,24]
Ti-6Al-4V	114	760 – 880	–	895 – 930	~80	[23,24]
Ti (grade 2)	102	275	–	390 – 540	–	[25–27]
Co-Cr alloy (ASTM F75)	210	448 – 517	–	655 – 889	–	[28]
Co-Cr alloy[a] (ASTM F562)	232	1500	–	1795	–	[28]
PLLA	2.7 – 4.14	–	58.6	15.5 – 150	–	[29–31]
Mg	41 – 45.5	51	65 – 100	175 – 235	15 – 40	[32–35]
Zn	90 – 110	285 – 325	–	90 – 200	–	[32,36]
Fe	204 – 212	108 – 122	–	230 – 345	–	[32,37,38]

[a] Property of cold worked and aged material.

exceptional machinability [4]. However, the main drawback lies in its slow corrosion rate as well as insoluble corrosion products [4]. Zn and its alloys have moderate corrosion rates and potential bioactivities [5,6]. However, the relatively low mechanical strength, strain softening behaviour, and high sensitivity of Zn ions for bioactivity remain challenges [7]. Therefore, Mg has been explored most extensively due to its excellent biocompatibility, biodegradation, and comprehensive mechanical properties [8–10]. The closer elastic modulus and density of Mg and its alloys (41 - 45 GPa, 1.74 - 2.0 g/cm^3) to those of bone (3 - 20 GPa, 1.8 - 2.1 g/cm^3) help in reducing the stress shielding effect in orthopaedic implant application [11]. In addition, Mg ions play a crucial role in bone metabolism as a beneficial bivalent ion [12]. They support the function of bone osteoclasts and aid in the formation of biological apatite. However, the rapid degradation of Mg with the evolution of hydrogen (H_2) gas in the physiological environment is the major challenge to be used as an implant material. The evolved H_2 gas leads to the formation of gas pockets next to the implant which separate the tissue layer and delay the healing process [13]. The lower mechanical strength of Mg is also a major concern because the implant needs to be strong enough to maintain its structural integrity during the degradation before the tissue is adequately healed.

To overcome these limitations, Mg based alloys with adequate mechanical strength along controlled degradation rate are developed by adding various alloying elements to Mg. Among all the Mg-based alloys, Mg-Al, Mg-Ca, Mg-Mn, Mg-RE (rare earth), and Mg-Zn alloys grab a lot of attention as potential biodegradable metals [8,14–16]. The addition of Al improves both the mechanical and corrosion performance of Mg-Al alloy, but the suspicion of Al involvement in Alzheimer disease limits its application [16]. Similarly, the addition of RE elements improves the mechanical properties and corrosion resistance, but the accumulation of RE phosphates and Nephrogenic Systemic Fibrosis caused by Gd compounds are also concerned [16]. In Mg-Ca alloy, the addition of Ca improves the mechanical properties and biocompatibility. The presence of Ca leads to more intermetallic Mg_2Ca phase formation which accelerate the corrosion process and also hinders the corrosion process by the early deposition of apatite. Therefore, this dual nature of Ca during corrosion process resulted a few reported literatures of *in vivo* data [8]. The intermediate electrode potential of Zn in between Mg and Fe resulted in the controlled degradation behaviour slower than pure Mg, that led to extensive research and development of Mg-Zn alloys [17–21]. In physiology, Zn is an essential element involved in various biological processes such as gene expression, signal transduction, nucleic acid metabolism, coordination of various organic ligand interactions, and apoptosis [15,22]. Therefore, Zn-containing Mg alloys have been paid more attention and developed as promising candidates for biomedical applications.

In this paper, the research work on the development of Mg-Zn alloy-based biomaterials and their advantages and limitations have been critically reviewed. The effect of alloying, processing techniques, and surface treatment on the microstructure, mechanical performance, degradation behavior, and biocompatibility have been discussed. The results of *in vitro* and *in vivo* evaluation of these alloys have also been summarized.

2. Processing techniques and microstructure of Mg-Zn alloy

The binary Mg-Zn phase diagram (Fig. 1) shows that the maximum solubility of Zn in Mg is 6.2 wt.% (*i.e.* 2.5 at.%) at the eutectic temperature of 341 °C [39]. However, there is a negligible solubility of Mg in Zn at room temperature. $Mg_{51}Zn_{20}$, $Mg_{21}Zn_{25}$, Mg_4Zn_7, $MgZn_2$, and Mg_2Zn_{11} are the stable compounds, and present in the phase diagram. $MgZn_2$ is a well-known non-stoichiometric compound, with a solubility limit of around 1 wt.% at around 416 °C and melts congruently at ~ 589 °C. The remaining compounds are stoichiometric in nature. The invariant reactions include one eutectoid reaction $Mg_{51}Zn_{20} \rightleftharpoons (Mg) + Mg_{21}Zn_{25}$ at 325 °C, two eutectic reactions $L \rightleftharpoons Mg_{51}Zn_{20} + Mg_{21}Zn_{25}$ at 341 °C, and $L \rightleftharpoons (Zn) + Mg_2Zn_{11}$ at 364 °C, four peritectic reactions $L + (Mg) \rightleftharpoons Mg_{51}Zn_{20}$ at 341 °C, $L + Mg_4Zn_7 \rightleftharpoons$

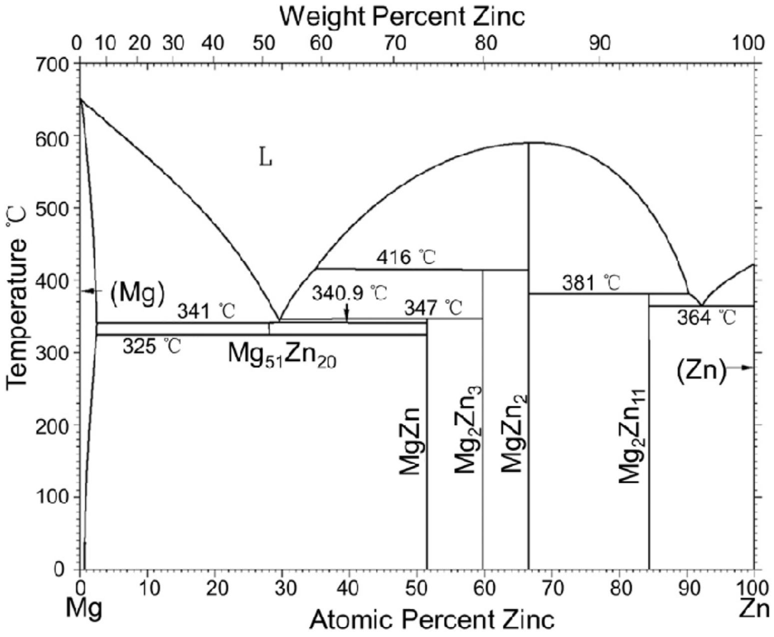

Fig. 1. The binary Mg-Zn phase diagram. Reprinted by permission from Springer Nature: Comment on Mg-Zn (magnesium-zinc), H. Okamoto, JPE 15, 129–130 (1994), https://doi.org/10.1007/BF02667700 [40].

$Mg_{21}Zn_{25}$ at 347 °C, L + $MgZn_2 \rightleftharpoons Mg_2Zn_{11}$ at 381 °C, and L + $MgZn_2 \rightleftharpoons Mg_4Zn_7$ at 416 °C.

2.1. Casting

As described above, the solubility of Zn in Mg is maximum as 6.2 wt.% at 341 °C and negligible at room temperature [39]. Therefore, the microstructure of as-cast Mg-Zn alloy consists of primary α-Mg matrix and secondary phases precipitating along grain boundaries. However, Cia et al. reported a single-phase microstructure for Mg-1Zn alloy [41]. Furthermore, Loftabadi et al. observed only the MgZn secondary phase for Mg-Zn alloy with Zn up to 3 wt.%, whereas the Mg-Zn alloy having Zn more than 6 wt.% has secondary MgZn phase + $Mg_{51}Zn_{20}$ intermetallic phase [42]. The $Mg_{51}Zn_{20}$ phase at grain boundaries is attributed to the non-equilibrium solidification. The increased Zn content resulted in an increase in the fraction of secondary phases which became non-uniformly distributed. In case of Mg-Zn alloy above 5 wt.% Zn, the second phase formed a network structure of dendrite along the grain boundaries (as shown in Fig. 2). In Mg-Zn alloy with low Zn content, however, dendritic structures with their sizes of 149 µm and 67 µm was observed in Mg-2Zn and Mg-4Zn alloys, respectively, where pure Mg showed dendritic structure sizes of 700 µm [43]. Furthermore, Peng et al. observed polygon (pentagon or hexagon) petal-shaped secondary dendrites and Mg matrix in all as-cast Mg–xZn (x = 0.5, 1, 1.5, 2 wt.%) alloys [44].

Grain size of Mg-Zn alloys decreased with an increase in Zn content up to 5 wt.% [41] or 6 wt.% [45], and after that, the refinement efficiency of Zn is not significant or decreased. The segregation of Zn at the front of grain growth forms an intensive constitutional undercooling in a diffusion layer ahead of the advancing solid/liquid interface. The Zn segregation restricts the grain growth, promoting the nucleation of the primary Mg, and thus, it refines the grain size [46]. The growth restriction factor (GRE) is higher for Zn (5.31) than Al (4.32) and Y (1.70), indicating that Zn has more powerful growth restriction and better refinement efficiency [47]. The grain sizes of various as-cast Mg-Zn alloys are summarized in Table 2.

2.2. Heat treatment

Researchers have employed different heat treatment processes to alter the microstructure of the Mg-Zn alloy. The microstructure with no second phase were reported for Mg-xZn (x = 1, 2, 3, 4, 5, and 6 wt.%) alloy after heat treatment at 380 °C for 10 h in air followed by water quenching [48]. In their study, the grain size was decreased from ~ 400 to ~ 300 µm with increase in the Zn content from 1 to 6 wt.% [48], which is attributed to the restriction of the grain growth with high Zn content, as explained in Section 2.1, promoting the nucleation of the primary Mg [46]. A similar observation of no dendrites with more uniform microstructure having a nearly equiaxed grain was reported after solution treatment (ST) at 400 °C for 10 h, followed by water quenching at room temperature on Mg-4Zn alloy [43]. The quenching process leads to insufficient time for grain growth and resulted in decreased grain size in the specimen. However, α-Mg matrix with secondary phases (*i.e.* $Mg_{21}Zn_{25}$, $Mg_{51}Zn_{20}$, and $MgZn_2$ intermetallic) were observed for Mg-12Zn alloy after annealing at 320 °C/20 h with subsequent quenching [49]. The presence of secondary phase may be attributed to the fact that Mg dissolves Zn up to 8 wt.% at this heat treatment temperature, and upon quenching the excess Zn was precipitated

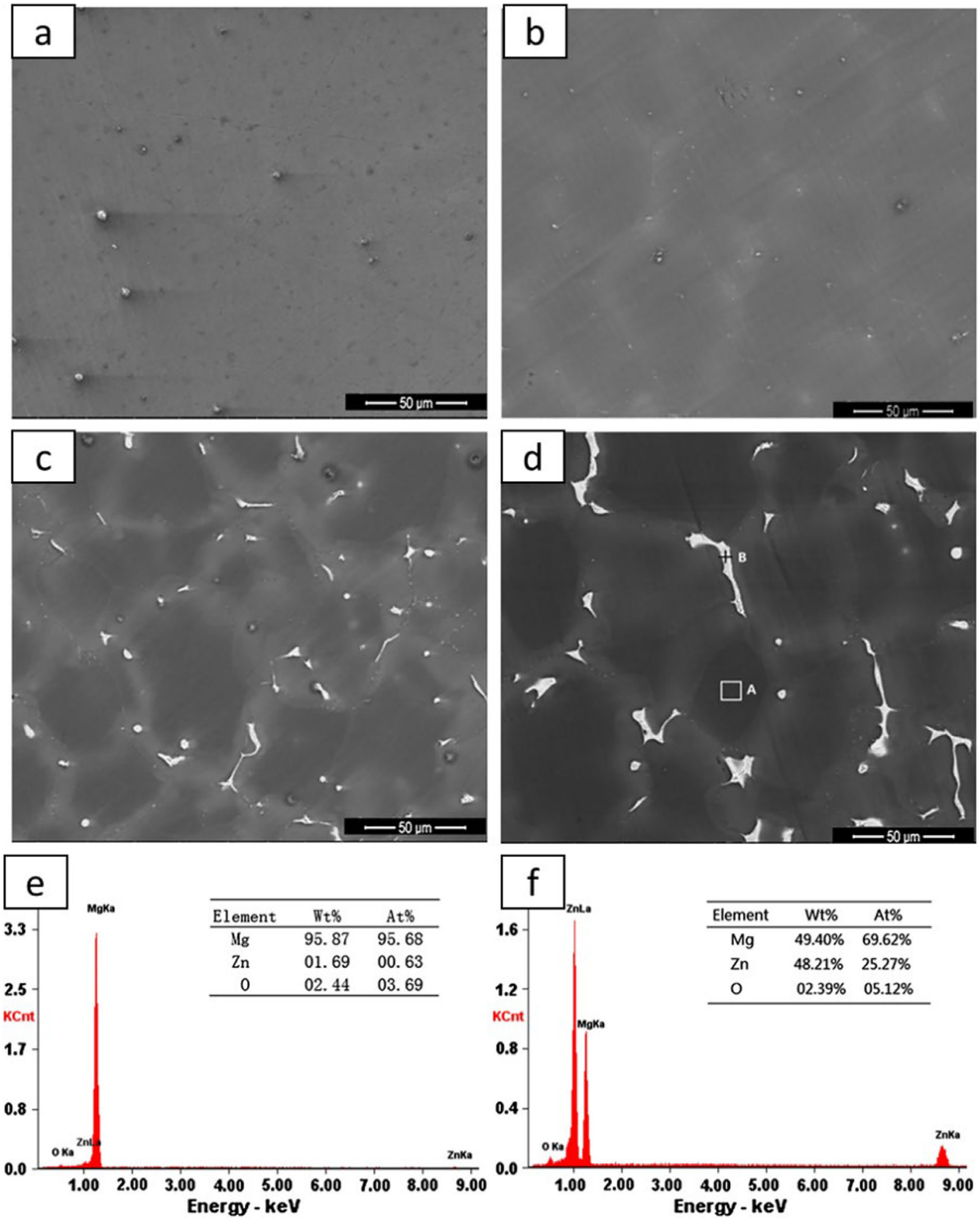

Element	Wt%	At%
Mg	95.87	95.68
Zn	01.69	00.63
O	02.44	03.69

Element	Wt%	At%
Mg	49.40%	69.62%
Zn	48.21%	25.27%
O	02.39%	05.12%

Fig. 2. The SEM micrograph showing the microstructures of (a) pure Mg, (b) Mg-1Zn, (c) Mg-5Zn, (d) Mg-7Zn, and EDS analysis corresponding to assigned area A (e) and B (f). Reprinted from Materials Science and Engineering: C, vol 32, Shuhua Cai, Ting Lei, Nianfeng Li, Fangfang Feng, Effects of Zn on microstructure, mechanical properties and corrosion behavior of Mg–Zn alloys, page no. 2570–2577, Copyright 2012, with permission from Elsevier [41].

as secondary phases. Therefore, the heat treatment temperature should be selected to completely dissolve the Zn content of the alloy in Mg at that temperature in order to obtain a single-phase microstructure.

Furthermore, grain growth with the disappearance of the dendrite structure consisting of α-Mg + MgZn was observed for Mg-3Zn alloy after ST at 310 °C for 24 h followed by water quenching [50]. This indicates that the prolonged heating period causes the grain growth of the alloy. The solution treatment followed by quenching is referred as T4 treatment and T4 treatment followed by aging is termed as T6 treatment. ST (160 °C for 7–102 h) and T6 treated Mg-4Zn alloys had grain growth as 76% and 94% of as-cast one, respectively [43]. Xian-bin et al. reported a similar trend in T4 and T6 Mg-3Zn alloys as their grain sizes of 240 µm and 300 µm, respectively, which are larger than that of as-cast one (120 µm) [51]. A homogeneous and decreased amount of secondary MgZn phases were observed in the T4 Mg-3Zn alloy,

Table 2
Summary of grain sizes and the mechanical properties of various as-cast Mg-Zn alloys.

Materials	Grain size (μm)	Modulus (GPa)	Yield strength (MPa)	Ultimate tensile strength (MPa)	Elongation (%)	Compression strength (MPa)	Hardness	References
Pure Mg	350	1.86	29.88	100.47	7.43	183.09	37.10 HB	[41]
	700	–	–	–	–	–	–	[43]
Mg-0.5Zn	185.2	–	–	–	–	–	–	[42]
	780	–	–	–	–	–	–	[66]
	600–800	–	–	–	–	–	–	[67]
	–	–	38 ± 4	95 ± 13	4.2 ± 1.8	–	–	[44]
Mg-1Zn	280	–	–	–	–	–	–	[54]
	640	–	–	–	–	–	–	[66]
	198.6 ± 28.9	–	–	–	–	–	–	[68]
	100	24.23	60.62	187.73	13.77	329.60	47.33 HB	[41]
	–	–	20 ± 2	101.5 ± 3	6.96 ± 0.5	–	–	[82]
	–	–	~ 28	~ 125	~ 18	–	–	[88]
	–	–	42 ± 3	99 ± 10	6.1 ± 1.9	–	–	[44]
	–	–	56	111.6	1.2	–	–	[69]
Mg-1.5Zn	–	–	51 ± 3	109 ± 8	5.9 ± 1.8	–	–	[44]
	250	–	–	–	–	–	–	[70]
Mg-2Zn	149	–	–	–	–	–	–	[43]
	580	–	–	–	–	–	–	[66]
	~500	–	–	–	–	–	–	[71]
	–	–	65 ± 3	121 ± 11	5.3 ± 1.9	–	–	[44]
	–	–	27 ± 2	145.9 ± 5	12.2 ± 1.5	–	–	[82]
Mg-2.65Zn	150	–	45	145	12	–	–	[72]
Mg-3Zn	135.5	–	–	–	–	–	–	[42]
	120	–	–	–	–	–	–	[51]
	490	–	–	–	–	–	–	[66]
	150–200	–	–	–	–	–	–	[67]
	–	–	47 ± 1.5	167.8 ± 10	13.7 ± 1.0	–	–	[82]
	–	–	–	–	–	–	48.8 ± 1.8 Hv	[50]
	86.7	–	76.5	166.6	9.3	–	–	[69]
Mg-4Zn	29	–	–	–	–		–	[43]
	–	–	58 ± 1.0	216.8 ± 15	15.8 ± 5.5	–	–	[82]
	–	–	–	156.93	7.38	–	–	[89]
Mg-5Zn	133.8	–	–	–	–	–	–	[65]
	88.8 ± 7.9	–	–	–	–	–	–	[68]
	55	36.47	75.60	194.59	8.50	334.12	53.80 HB	[41]
	129	–	120	212	10	–	52 Hv	[73]
	–	–	68 ± 1.5	185 ± 5	9.2 ± 0.5	–	–	[82]
	56.9	–	77.6	188.6	7.7	–	–	[69]
Mg-6Zn	–	–	69 ± 1.5	182 ± 5	7.2 ± 0.5	–	–	[82]
Mg-7Zn	70.3 ± 6.4	–	–	–	–	–	–	[68]
	56	39.60	67.28	135.53	6.00	353.11	56.26 HB	[41]

whereas in the T6 Mg-3Zn alloy, more precipitates formed on matrix and grain boundaries as chain structure [51]. However, no secondary Mg_xZn_y phase was observed in T4 (450 °C for 2 h followed by water quench at room temperature) Mg-5Zn alloy, whereas T6 (T4 + aging at 230 °C for 4, 6, and 10 h followed by cooling in air) Mg-5Zn alloy showed the Mg_xZn_y secondary phases uniformly precipitated on the grain boundaries, whose dimensions became smaller than that in the as-received Mg-5Zn alloy [52]. The quenching process in T4 treatment gives insufficient time to precipitate, resulting in the decreased or no secondary phase, whereas the slow cooling in T6 treatment resulted in higher number of secondary phase precipitates. Additionally, many short bar, white precipitation phases were observed inside the crystal grains of T6 Mg-5Zn alloy [52]. With an increase in aging time from 4 to 10 h for T6 Mg-5Zn alloy, there was no change in the characteristics of second phase precipitates at grain boundaries [52], because of grain boundary hinderance for the growth. However, the short bar, white precipitation phases within the crystal grains increases [52] due to no obstruction during the growth. The precipitation phases present a filament characteristic with an approximate length of 2 μm [52]. The precipitation phases grow along the same direction in one crystal grain, but different directions in different crystal grains [52]. With the increase in aging time from 10 h to 144 h for T6 Mg-3Zn alloy, the volume fraction of the precipitation phase increased from 0.04 ± 0.02% to 3.03 ± 0.17%, with the growth of rod shape precipitates [50].

In the case of Mg-xZn ($x = 3$, 6 wt.%) alloys with T4 solid solution heat treatment at 340 °C for 6, 12, and 18 h followed by hot water quenching at around 50 °C, the microstructure remained unchanged with an almost similar amount of secondary $Mg_{12}Zn_{13}$ phases in both as-cast and T4 treated Mg-3Zn alloys [53]. However, in T4 Mg-6Zn alloy after 6 h, the number of precipitates significantly changed, indicating the decomposition of the secondary phase ($Mg_{51}Zn_{20}$) into the matrix and $Mg_{12}Zn_{13}$ [53]. An increase in the heat treatment time to 12 and 18 h causes no significant change in the amount of secondary phases [53], which can also be attributed to the increase in Zn solubility in Mg up to 8 wt.% at the heat treatment temperature.

In summary, the literature indicates that the heat treatment temperature, time, and cooling method influence the microstructure. The heat treatment temperature should be above 340 °C as MgZn precipitates are unstable and would be dissolved in the matrix at temperatures higher than about 340 °C according to the Mg-Zn phase diagram (Fig. 1). The T4 treatment is more suitable than the T6 treatment to obtain optimized microstructure with controlled grain size and uniform distribution of the secondary phase, because the aging gives the continuous secondary phase which may be detrimental for corrosion properties. The T4 treatment time up to 6 h would be most promising, as beyond 6 h, less significant changes were observed in the microstructure of Mg-Zn alloys. Additionally, prolonged aging time in T6 specimens resulted more dispersion of secondary phases in the crystal grain which grow monotonically with time. The quenching process leads to insufficient time for grain growth and precipitation of secondary phases, resulting in decreased grain size with reduced or no precipitation of secondary phases in the specimen. The solubility limit at the heat treatment temperature along with the cooling process influences the secondary phase in the microstructure. For similar conditions of heat treatment, the grain size decreases with an increase in Zn content up to 6 wt.% with no significant effect on the secondary phases, whereas for Zn content > 6 wt.% needed investigation.

2.3. Deformation techniques

As Mg-Zn alloys have excellent processability, various deformation techniques have been applied to modify the microstructure of the Mg-Zn alloy. A microstructure having recrystallized grain structure comprising equiaxed grains were observed after rolling on Mg-1Zn [54] and Mg-3Zn [55] alloys. The grain size of the specimens decreases by 82.62% with an increase in the number of cycles from 0 to 5 [55]. However, fine homogenous dynamic recrystallization (DRX) grains with intermetallic phase were observed after performing a high strain rate rolling process (HSRR) on Mg-4Zn alloy [56]. The intermetallic phase after HSRR is attributed to the stress-induced precipitation during HSRR.

Similar to (relatively low strain rate) rolling, uniform equiaxed grains with no second phase were observed for hot extruded Mg-Zn alloy with Zn up to 6 wt.%. [57,58]. Grain refinement was not observed with an increase in Zn content [58,59]. In contrast to this, Peng et al. reported grain refinement in backward extruded Mg-Zn alloy with an increase in Zn content from 0.5 to 2 wt.% [44]. Inhomogeneous microstructure with white precipitates were also observed in extruded Mg-xZn (x = 2, 3, 4, and 5 wt.%) alloy [60]. The second phases (Mg_xZn_y) present a discrete distribution along the grain boundaries and their volume fractions gradually rise with increasing Zn concentration from 2 to 5 wt.% [60]. The secondary phases, with the help of the pinning effect, prevent the growth of DRXed grains and resulted in a fine microstructure in the deformed sample [43]. Inhomogeneous microstructure having fine equiaxed grains and row elongated grains with plenty of strike-like and coarse intermetallic phases were also observed along the extrusion direction in sintered + hot extruded Mg-6Zn alloy [61]. The intermetallic phases become coarser with an increase in Zn content [61]. Hot extrusion and multi-directional forging (MDF) reduced the grain size of Mg-4Zn alloy to 80% and 73% of as-cast one, respectively [43]. The volume fractions of the precipitates in extruded and MDF processed specimens are 0.4% and 0.6%, respectively, which are lower than that of the as-cast one (1.3%) [43].

Severe plastic deformation techniques were also employed to refine the microstructure of Mg-Zn alloy. Equal-channel angular pressing with applied back pressure (ECAP-BP) up to 4 passes on Mg-xZn (x = 6, 12 wt.%) alloy resulted in the microstructure consisted of highly-deformed and partially-recrystallized regions with $MgZn_2$ and $Mg_{21}Zn_{25}$ particles [62]. The ECAP-BP Mg-12Zn alloy showed a majority of the Zn from the supersaturated solid solution of the α-Mg matrix, which is consumed mainly by the $MgZn_2$ nanoparticles, resulting in the inhomogeneous distribution of Zn in the α-Mg matrix [62]. The $Mg_{21}Zn_{25}$ microparticles in Mg-12Zn exhibited distinct forms in the α-Mg matrix that were characterized as a single-crystalline form, a nano-crystalline form, and a broken-up form [63]. Differences in the size of $MgZn_2$ nanoparticles were reported in the α-Mg matrix of ECAP-BP Mg-12Zn alloy [64]. The $Mg_{21}Zn_{25}$ particles were observed in a highly deformed α-Mg matrix [64]. Friction stir processing (FSP) on Mg-5Zn alloy resulted in uniform, fine grain of size 1.3 µm, whereas the cast Mg-5Zn alloy showed non-uniform, coarse grain of 133.8 µm [65]. The Large precipitates in as-cast specimens were broken down into refined and uniformly distributed precipitates after FSP.

The microstructure of the specimen after the deformation process has resulted in grain refinement (Fig. 3). The grain sizes of various Mg-Zn alloys resulting from different processing methods are summarized in Table 3. In some cases, the inhomogeneity of the microstructure of the deformed specimens has been observed, which is related to the non-equal rate of dynamic recrystallization in different grains, and thus, DRX is found to be incomplete in some grains.

3. Mechanical properties of Mg-Zn alloy

As described earlier in Section 1, the appropriate mechanical properties of the temporary implant are a fundamental requirement to maintain its structural integrity during the degradation process before the tissue is adequately healed. Due to the insufficient mechanical properties of pure Mg, al-

Table 3
Summary of grain sizes and the mechanical properties of various deformed Mg-Zn alloys.

Materials	Processing methods	Grain size (μm)	Modulus (GPa)	Yield strength (MPa)	Ultimate tensile strength (MPa)	Elongation (%)	Compression strength (MPa)	Hardness (Hv)	References
Pure Mg	Hot pressed at 28 MPa for 1–2 h at 535 °C	242.6	–	–	–	–	–	–	[83]
Mg-0.4Zn	Hot rolled (at 450 °C) + Annealed	60	–	–	–	–	–	–	[74]
Mg-0.5Zn	Back extruded at 420 °C with an extrusion ratio of 12.25	47.5	–	62 ± 1	145 ± 8	17.2 ± 1.3	–	–	[44]
Mg-1Zn	Back extruded at 420 °C with an extrusion ratio of 12.25	37.5	–	91 ± 1	169 ± 9	18.7 ± 1.4	–	–	[44]
	Hot extruded at 300 °C with an extrusion ratio of 25:1	17.9	–	116	254	16.2	–	–	[58]
	hot rolling (at 400 °C) + annealing (at 400 °C for 5 min)	11	–	–	–	–	–	–	[54]
	Hot extruded at 400 °C	35.3							[75]
	Hot Rolled at 400 °C	–	–	~ 160	~ 240	~ 23	–	–	[88]
Mg-1.5Zn	Back extruded at 420 °C with an extrusion ratio of 12.25	36	–	101 ± 1	190 ± 7	17.2 ± 1.5	–	–	[44]
	hot rolling (at 250 °C) + annealing (at 350 °C for 1 h)	25.82	–	–	–	–	–	–	[70]
	hot rolling (at 350 °C) + annealing (at 350 °C for 1 h)	20.85	–	–	–	–	–	–	[70]
	hot rolling (at 450 °C) + annealing (at 350 °C for 1 h)	27.1	–	–	–	–	–	–	[70]
Mg-2Zn	Back extruded at 420 °C with an extrusion ratio of 12.25	–	–	111 ± 1	198 ± 6	15.7 ± 1.6	–	79	[44]
	Hot extruded at 300 °C with an extrusion ratio of 25:1	–	–	109	258	16.4	–	–	[58]
Mg-2.4Zn	Hot extruded at 210 °C with an extrusion ratio of 18:1	15	–	–	–	–	–	–	[94]
Mg-2.9Zn	Hot pressed at 28 MPa for 1–2 h at 535 °C	106.5	–	–	–	–	–	–	[83]
Mg-3Zn	Hot extruded at 300 °C with an extrusion ratio of 25:1	17.9	–	98	276	18.5	–	–	[58]
Mg-3.3Zn	Hot pressed at 28 MPa for 1–2 h at 535 °C	155.6	–	–	–	–	–	–	[83]
Mg-4Zn	Hot extruded at 300 °C with an extrusion ratio of 25:1	17.6	–	89	297	20.6	–	–	[58]
	Hot extruded at 350 °C with an extrusion ratio of 11:1		–	198.4 ± 3.4	301.1 ± 4.1	33.9	–	44.5 ± 3.3	[90]
	Hot extruded at 350 °C with an extrusion ratio of 9:1	7.6 ± 2.6	–	–	–	–	–	–	[76]
	MDF (after 3 pass)		–	142	228	8	–	84	[91]
	MDF (after 5 pass)	2.3	–	135	196	8.7	–	–	[91]
	High strain rate rolling (HSRR)	4.5	–	–	–	–	–	–	[56]
	Hot pressed at 28 MPa for 1–2 h at 535 °C	70.2	–	–	–	–	–	–	[83]
Mg-4.4Zn	Hot pressed at 28 MPa for 1–2 h at 535 °C	112.9	–	–	–	–	–	–	[83]
Mg-5Zn	FSP	1.3	–	–	–	–	–	–	[65]
	Extruded	33.6	–	–	–	–	–	–	[60]

(*continued on next page*)

Table 3 (*continued*)

Materials	Processing methods	Grain size (μm)	Modulus (GPa)	Yield strength (MPa)	Ultimate tensile strength (MPa)	Elongation (%)	Compression strength (MPa)	Hardness (Hv)	References
Mg-6Zn	MDF (after 1 pass)	72 ± 4	–	130 ± 6	222 ± 10	8.3 ± 1	–	78 ± 6	[84]
	MDF (after 3 pass)	28 ± 2	–	145 ± 6	230 ± 10	6.2 ± 0.7	–	86 ± 6	[84]
	MDF (after 5 pass)	3.8 ± 0.5	–	138 ± 7	193 ± 9	7 ± 0.9	–	82 ± 5	[84]
	Hot extruded at 250 °C		42.3 ± 0.1	169.5 ± 3.6	279.5 ± 2.3	18.8 ± 0.8	433.7 ± 1.4	–	[57]
	Rolling		–	91.3 ± 40	124.1 ± 37.9	0.5 ± 0.3	–	48.32 ± 1.5	[92]

loying and microstructure control are major solutions to improve them. For Mg-Zn alloys, their hardness was reported to increase with an increase in Zn content (shown in Fig. 4) [42,44,45,79]. In Mg-Zn alloy with Zn content < 5 wt.%, the increased hardness is due to the solid solution strengthening of Zn dissolved in the Mg matrix [42]. However, in Mg-Zn alloy with Zn content > 5 wt.%, the hardness enhancement is attributed to the evolution of the secondary phase ($Mg_{51}Zn_{20}$) at the grain boundary in addition to the MgZn intermetallic phase [80]. The increased hardness with increased Zn content in Mg-Zn alloy indicate the probability of decrease in the wear of the implant [81]. Furthermore, the tensile and compressive strength was improved up to 5 wt.% Zn due to grain strengthening, solid solution strengthening, and second phase strengthening [41]. The decreased strength above 5 wt.% Zn is attributed to plenty of secondary phases which formed a network structure with dendritic segregation along grain boundaries, resulting in residual defects and deteriorated strength and elongation of the specimen. The Zn-rich regions in Mg-Zn alloy were also often prone to the formation of microporosity, resulting in reduced mechanical properties. Some researchers [43,82,83] reported a similar trend of improved mechanical properties but up to 4 wt.% Zn, and over that, they declined. Therefore, the Mg-Zn alloy with 4 wt.% Zn having highest strength and hardness is more suitable as an implant material to prevent fractures and improve functional stability [81].

The alteration in microstructure due to heat treatment also influences the mechanical properties. For Mg-4Zn alloy, an increase in aging time from 0 to 62 h enhances the Vickers hardness from 27 to 41 due to the precipitation of more $MgZn_2$ phase [43]. However, decreased USS was reported for ST Mg-4Zn alloy due to the grain growth and dissolution of the precipitates [43].

The mechanical properties were further improved after the deformation process due to grain refinement (Fig. 5). For

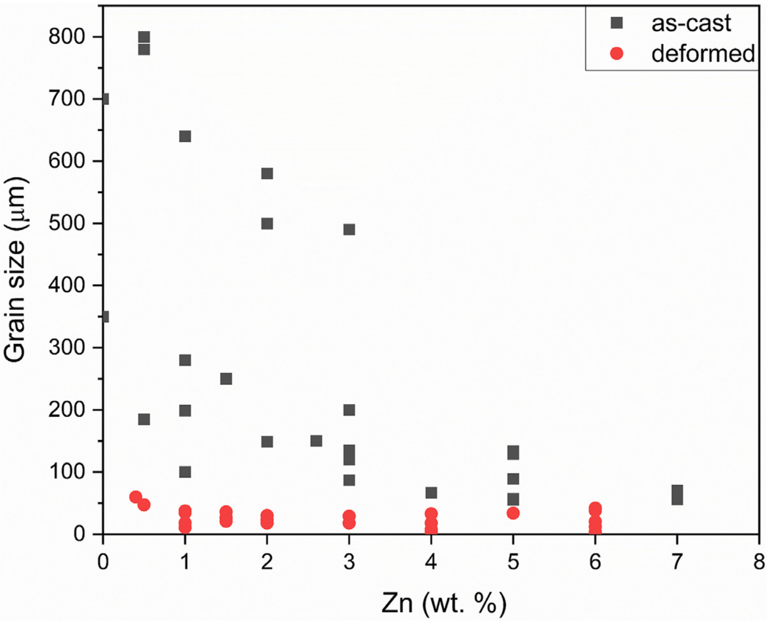

Fig. 3. The comparison of the grain size distribution for various as-cast and deformed Mg-Zn samples. The data sources are following references: as-cast from [41–43,51,54,65–73], and deformed from [43,44,56,58,60,70,74–78].

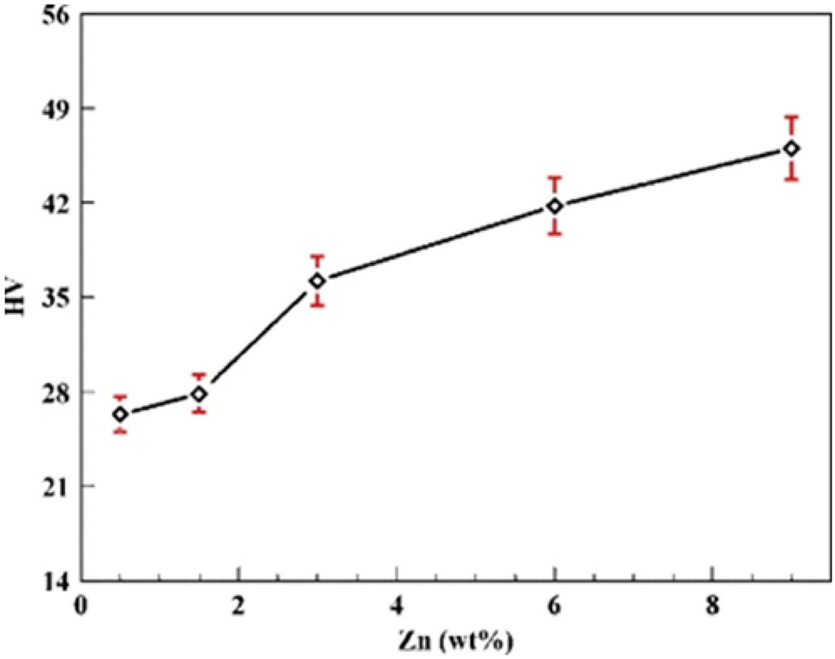

Fig. 4. The effect of different Zn additions on microhardness properties of Mg-xZn alloy. Reprinted by permission from Springer Nature: Rare Metals, Thermal characteristics and corrosion behaviour of Mg–Zn alloys for biomedical applications, LOTFABADI A.F., IDRIS M.H., OURDJINI A., KADIR A., FARAHANY S., and BAKHSHESHI-RAD H.R., Bull Mater Sci 36, 1103–1113 (2013), https://doi.org/10.1007/s12034–013–0566–9, Copyright 2013 [42].

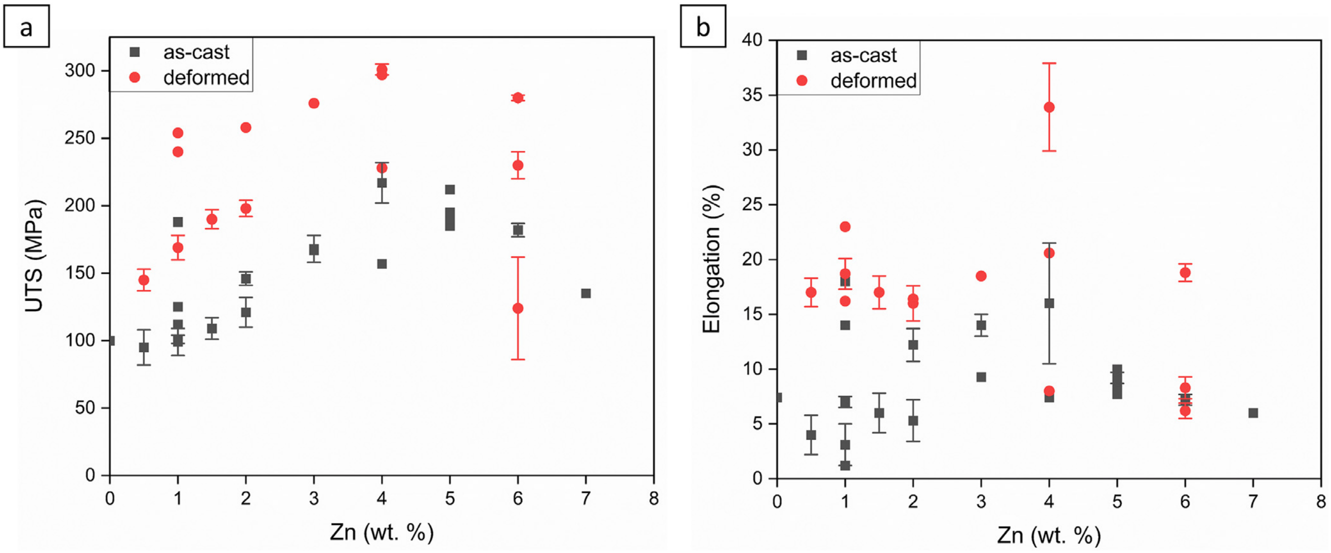

Fig. 5. The comparison of (a) UTS, and (b) elongation of various Mg-Zn alloys in as-cast and deformed conditions. The data sources are following references: as-cast from [41,44,69,73,82,88,89], and deformed from [44,57,58,84,88,90–92].

Mg-4Zn alloys, extrusion and MDF improved USS by 26% and 18%, respectively, than that of the as-cast one, due to their fine microstructure [43]. The enhanced properties are attributed to higher strain, grain refinement strengthening, and dispersion strengthening mechanisms.

In case of Mg-6Zn alloy, the hardness and strength were enhanced up to 3 passes of the MDF, and over 4 passes, they decreased due to dynamic recrystallization resulting in twin density reduction [84]. For the hot extruded specimens, an increase in Zn content from 1 to 4 wt.% decreased YS along with increased UTS and elongation [58]. This enhancement of elongation and decrease of YS might be attributed to the decrease in basal texture intensity with increase in Zn content, whereas the increase of UTS is considered to relate with the enhanced strain hardening ability [85,86]. Researchers also reported improved mechanical properties after ECAP-BP [62], and hot rolling [55,87] on Mg-Zn alloys.

Degradable implant materials have deterioration in the mechanical properties during their degradation process. Tensile test in 0.9 wt.% NaCl solution revealed about 19% loss in strength for the HSRR Mg-4Zn specimen after 7 days of immersion, while that of the as-cast sample is about 62% [56]. The tensile test in simulated body fluid (SBF) reported that Mg-4Zn alloy is susceptible to stress corrosion cracking at or below strain rates of 3.6×10^{-4} s^{-1} with approximately 10% loss in fracture stress as compared to that tested in air [93]. The Mg-4Zn alloy is found to crack at corrosion pits dominantly by anodic dissolution and hydrogen embrittlement.

In summary, the above literature indicates that the Zn content has to be controlled to promote the mechanical properties of Mg-Zn alloys more suitable for human implant materials. The Zn content up to 4 wt.% enhances the mechanical properties due to grain strengthening, solid solution strengthening, and second-phase strengthening mechanisms. The heat treatment temperature, time, and cooling process affect the mechanical properties. Similarly, the strain rate, the extent of grain refinement, and the dispersion of the secondary phase after the deformation process alter the mechanical properties. Table 2 and 3 show the grain size and various mechanical properties, tensile strength, ultimate tensile strength, compressive strength, and elongation, of different as-cast or deformed Mg-Zn alloys, respectively.

4. Degradation properties of Mg-Zn alloy

In the human body, a biodegradable implant is expected to degrade at a suitable rate matching to the recovery rate of injured tissues. Hence, it is essential to understand its degradation process and underlying mechanisms, together with the techniques to regulate degradation behaviour.

4.1. Degradation mechanism of Mg-Zn alloy

It is well known that the microstructure influences the corrosion behaviour of Mg and its alloys. The corrosion process initiated on the α-Mg matrix phase includes reactions (1) and (2) [95,96]. In Mg-Zn alloy, the lower standard electrode potential of Mg (−2.36 V) than Zn (−0.76 V) resulted in more release of Mg^{2+} than Zn^{2+} in an aqueous medium. The anodic dissolution of Mg released Mg^{2+}, whereas the cathodic reaction evolved hydrogen gas (H_2) and released hydroxide ions (OH^-) resulting in an increase in local pH. According to the Pourbaix diagram, the released Mg^{2+} reacts with OH^-, resulting in magnesium hydroxide [$Mg(OH)_2$] formation at pH > 11.5. However, after surgery, the pH is nearly 7.4 or lower at the interface of bone and implant due to circulation, metabolic, and resorptive processes [97]. As a result, a partially protective, unstable $Mg(OH)_2$ layer was formed on the alloy surface. With the progress of time, the $Mg(OH)_2$ layer becomes denser which inhibits the ion penetration through the layer, retarding the growth of it. Therefore, the dissolution-precipitation mechanism plays the predominant role in the growth of $Mg(OH)_2$ layer [98].

The released Zn^{2+} can also react with OH^- to form $Zn(OH)_2$ [99–101]. The solubility product constant of $Zn(OH)_2$ is much smaller than that of $Mg(OH)_2$ [102] and $Zn(OH)_2$ is converted to more stable ZnO (reaction (5)), which can enhance the protectiveness of the insoluble salt layer (ISL) [59,101]. The chloride ion (Cl^-) in the physiological fluids reacts with the deposited $Mg(OH)_2$ and dissociates it by forming $MgCl_2$ (reaction (4)). The smaller radius of Cl^- enables to penetrate through ISL which causes its preferential adsorption by replacement of OH^- [61]. As a result, Cl^- shifts the dynamic balance between the dissolution and formation of ISL, resulting in acceleration of the corrosion rate. The presence of Ca^{2+}, CO_3^{2-} and PO_4^{3-} in the physiological fluids results in the predominant deposition of calcium/magnesium phosphate/carbonate on the specimen surface due to their lower solubilities, which further retards the anodic dissolution of Mg.

$$\textit{Anodic reaction}: \ Mg\ (s) \rightarrow \ Mg^{2+}(aq) \ + \ 2e^- \tag{1}$$

$$\textit{Cathodic reaction}: \ 2H_2O \ + \ 2e^- \ \rightarrow \ H_2(g)\uparrow \ + \ 2OH^-\ (aq) \tag{2}$$

$$Zn\ (s) \rightarrow \ Zn^{2+}(aq) \ + \ 2e^- \tag{3}$$

$$Mg(OH)_2\ (s) \ + \ 2Cl^-\ (aq) \ \rightarrow \ MgCl_2\ (s) + 2OH^-\ (aq) \tag{4}$$

$$Zn(OH)_2(s) \rightarrow ZnO + \ H_2O \tag{5}$$

The selection of *in vitro* physiological solution plays an important role in evaluating the degradation behaviour. In the human body, interstitial fluid has a similar composition to blood plasma; plasma penetrates through the capillary vessel wall to be interstitial fluid, which comes back to plasma via lymph flow. Hence, the *in vitro* physiological solution should have a similar composition to that of blood plasma. The physiological solution should contain essential components such as inorganic ingredients, organic components, and buffering system, since this influence severely the degradation behaviour of biodegradable metals [14]. Table 4 represents the list of common physiological solution and their ionic concentrations along with that of human blood plasma. As described above, the Cl^- and SO_4^{2-} contributes to the dissociation of $Mg(OH)_2$ layer, accelerating the degradation process [103] whereas HPO_4^{2-}/PO_4^{3-}, HCO_3^-/CO_3^{2-}, and Ca^{2+} retard the degradation process by the precipitation of their salts [103,104].

The deposition of the ISL on the specimen surface depends on the local pH of the corrosion environment. Since OH^- is released accompanying to Mg anodic dissolution, the buffering ability of the physiological solution severely influences the ISL deposition. The pH of the blood is maintained as 7.4 mainly by carbonate buffer system under the atmosphere of 5% CO_2, which is higher than that in air (0.4%) [105]. Therefore, the employment of carbonate buffer is necessary as the main buffer system in the physiological solution for evaluating the corrosion behaviour of Mg alloys. Because of this reason, phosphate buffered saline (PBS) is not preferable even though its pH was around 7.4. SBF and HBSS contains

Table 4
The main components of commonly used simulated physiological solutions in comparison with human blood plasma.

Medium	Na^+ (mM/L)	K^+ (mM/L)	Ca^{2+} (mM/L)	Mg^{2+} (mM/L)	Cl^- (mM)	HCO_3^- (mM/L)	$H_2PO_4^-/HPO_4^{2-}/PO_4^{3-}$ (mM/L)	SO_4^{2-} (mM/L)	Amino acids (g/L)	Vitamins (g/L)	Proteins (g/L)	Glucose (g/L)	Phenol red (mM/L)	Ref
Blood plasma[a]	142.0	5.0	2.5	1.5	103.0	27.0	1.0	0.5	0.25 −0.4	unknown	63 −80	0.65 −1.1	–	[104 [108–111]
PBS	154	4.1	–	–	140.6	–	9.5	–	–	–	–	–	–	[112]
SBF	142	5.0	2.5	1.5	148.8	4.2	1.0	0.5	–	–	–	–	–	[108]
Revised SBF[b]	142	5.0	2.5	1.5	103	27	1.0	0.5	–	–	–	–	–	[108]
HBSS	143	5.8	1.26	0.90	146.7	4.2	0.78	0.4	–	–	–	1.0	0.03	[113–115]
EBSS[b]	144.4	5.3	1.8	0.8	126.2	26.2	1.0	0.8	–	–	–	1.0	0.03	[116]
MEM[b]	143	5.4	1.8	0.8	125	26.2	1.0	0.8	0.87	0.008	–	1.0	0.03	[110,118]
EMEM[b]	144	5.4	1.8	0.8	125	26.2	0.9	0.8	0.86	0.009	–	1.0	0.02	[104]
DMEM[b]	157	5.3	1.8	0.8	121.1	44.0	0.9	0.8	1.61	0.032	–	4.5	0.04	[119,120]
α-MEM[b]	144.8	5.3	1.8	0.8	128.2	26.2	1.0	0.8	1.27	0.060	–	1.0	0.03	[117]

The compositions of the simulated body fluids (except SBFs) are based on the basic version of the commercially available products. The catalogue number of a representative one is shown in the brackets for reference. PBS: Dulbecco's phosphate buffered saline (ThermoFisher Scientific 14190), SBF: simulated body fluid, HBSS: Hanks' balanced salt solution (ThermoFisher Scientific 24020); EBSS: Earle's balanced salt solution (ThermoFisher Scientific 24010); MEM: Minimum Essential Medium (ThermoFisher Scientific 11095), EMEM: Eagle's Minimum Essential Medium (AccuDia^{TM} Eagle's MEM①); DMEM: Dulbecco's Modified Eagle's Medium (ThermoFisher Scientific 11965), α-MEM: Minimum Essential Medium alpha (ThermoFisher Scientific 12561).

[a] Being equilibrated with 5% CO_2.

[b] Should be used under 5% CO_2 atmosphere.

bicarbonate, but its concentration is much lower than that in plasma for their use in air, not under 5% CO_2, suggesting their inadequacy for the use as corrosion testing solution for preclinical evaluation. The simple buffering system such as Tris–HCl, maintains the pH of the corrosion testing solution low, inhibits the ISL formation, and accelerates the Mg dissolution [106].

Protein retards the Mg degradation in the initial stage and the effect weaken dramatically with the prolonged period [106]. Organic molecules like amino acids reduce ISL on the specimen surface, resulting in acceleration of Mg corrosion [104]. Cell culture media supplemented with protein mixture such as serum along with 5% CO_2 condition are regarded as the most suitable physiological solution for evaluating the Mg degradation behaviour [107]. Among them, EMEM or MEM-Earle is preferable since it was developed based on the composition of human blood plasma, that is, it has the closest composition. DMEM, one of the modified MEMs, contains almost double amount of $NaHCO_3$ than that of blood plasma, suggesting the acceleration of carbonate precipitation in ISL as well as its buffering ability exceeding that in the human interstitial fluid. The appropriateness of this high $NaHCO_3$ concentration of DMEM should be studied in comparison to *in vivo* or clinical data.

4.2. Effect of amount of Zn on the degradation of Mg-Zn alloy

In Mg-Zn alloys, the concentrations of Zn and the nature of the secondary phase have a significant role in their degradation behaviour. The degradation rate decreases with an increase in Zn content up to 5 wt.%, but over that, it increases [41–43,45,53]. The increase of Zn content over 5 wt.% increased continuous network structure of intermetallic MgZn phase in the matrix, leading to the formation of anode-cathode sites and resulting galvanic corrosion. Mg-Zn alloys always have a lower degradation rate than pure Mg [41,43,121]. The surface of pure Mg (as shown in Fig. 6) collapsed severely and showed lamellar microstructures in SBF (a corrosion media), indicating a substantial corrosion rate during the immersion test [41]. The surface of Mg-Zn alloys showed several deep pits (indicated by arrows) superimposed on superficial corrosion over the specimen surfaces, implying localized corrosion attacks during the immersion process in SBF [41]. The localized corrosion for Mg-Zn alloy was also confirmed from the breakdown potential (E_b) (as shown in Fig. 7) on the polarization curve obtained by the electrochemical test in SBF. The more positive E_b indicates less risk of localized corrosion [122], where Mg-5Zn alloy showed slightly higher E_b (= -0.96 V in Fig. 7) than those of Mg-1Zn alloy ($E_b = -1.09$ V) and Mg-7Zn alloy ($E_b = -1.25$ V).

Additionally, the electrochemical impedance spectroscopy (EIS) of Mg-Zn alloys suggests the involvement of two-time constants at the high-frequency region (HF) and the low frequency region (LF) (as shown in Fig. 8) [41], suggesting the interference of ISL formed on the Mg-Zn alloy surface during the immersion in SBF. The capacitive loop in the high fre-

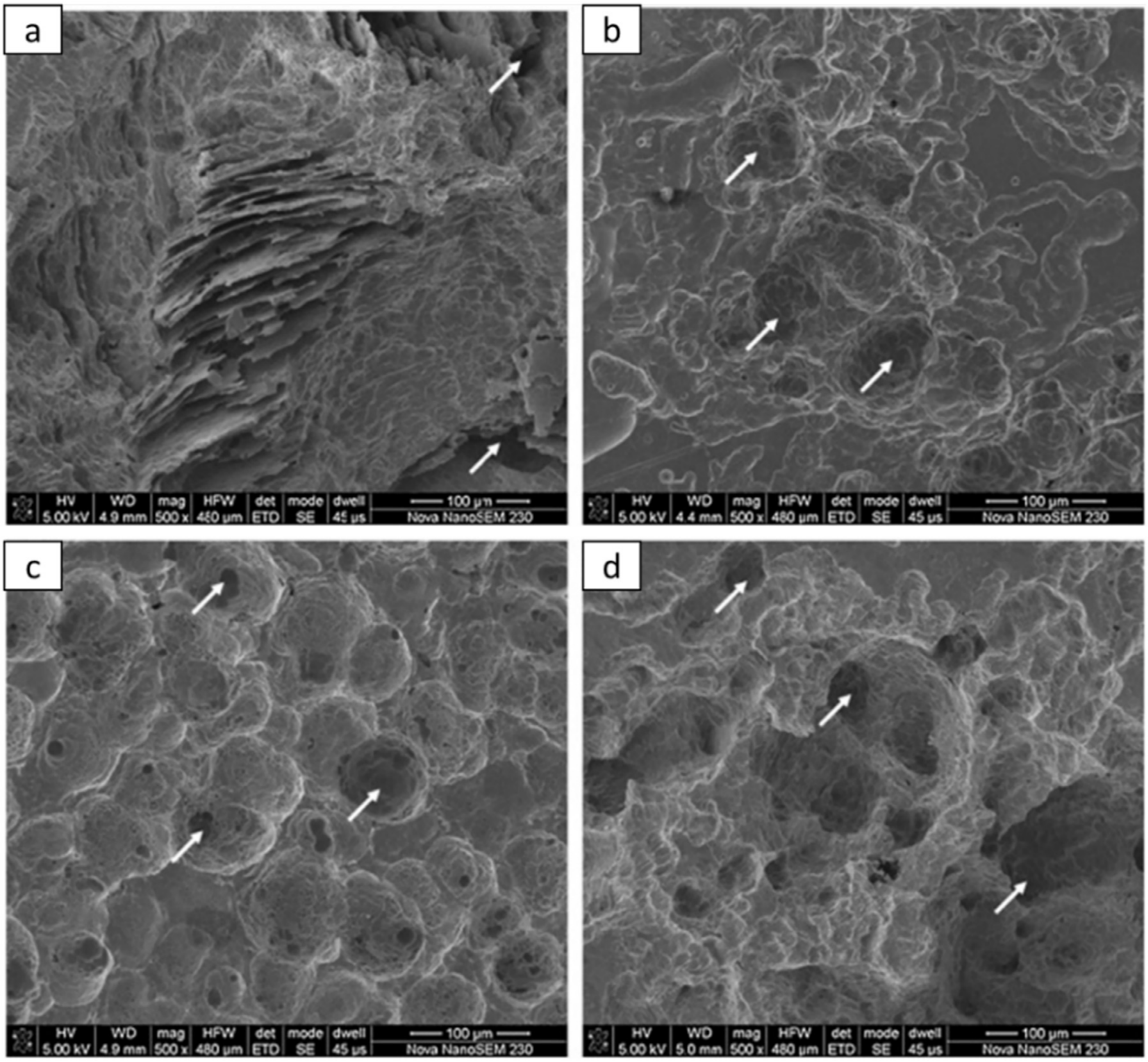

Fig. 6. The SEM microstructure of corroded appearance after corrosion product removal for (a) pure Mg, (b) Mg–1Zn, (c) Mg–5Zn and (d) Mg–7Zn immersed in SBF for 5 days. Reprinted from Materials Science and Engineering: C, vol 32, Shuhua Cai, Ting Lei, Nianfeng Li, Fangfang Feng, Effects of Zn on microstructure, mechanical properties and corrosion behavior of Mg–Zn alloys, page no. 2570–2577, Copyright 2012, with permission from Elsevier [41].

quency region can be attributed to the charge transfer reaction at the metal surface and the capacitance of the electric double layer formed at the interface between the metal surface and the corrosive medium. The capacitive loop in the low frequency region can be attributed to the mass transport in the solid phase, such as the diffusion of ions through the insoluble salt layer. The EIS analysis also confirms the lower degradation rate of Mg-Zn alloys than pure Mg. Table 5 shows the corrosion rate of as-cast pure Mg and Mg-Zn alloys in various physiological solutions.

4.3. Effect of heat treatment on the degradation of Mg-Zn alloy

It has been reported that heat treatment alters the microstructures which play a pivotal role in tailoring the degradation rate of Mg-Zn alloys. T4 Mg-6Zn alloy has a higher reduction rate in corrosion than T4 Mg-3Zn alloy in comparison to those of corresponding as-cast alloys [53]. Although the as-cast Mg-6Zn alloy (having $Mg_{12}Zn_{13}$ and $Mg_{51}Zn_{20}$ phases) showed higher corrosion rate than as-cast Mg-3Zn alloy (having $Mg_{12}Zn_{13}$ phases), the decomposition of $Mg_{51}Zn_{20}$ in T4 Mg-6Zn alloy resulted in the lower corrosion rate than the T4 Mg-3Zn alloy [53]. The increased heating time in T4 process from 6 to 18 h has a less significant influence on the corrosion behaviour on all the Mg-Zn alloys due to the unchanged microstructure after heat treatment beyond 6 h [53]. The improving effect of solution treatment on corrosion resistance was also confirmed by other studies. ST Mg-3Zn alloy gave a lower corrosion rate (3.05 ± 0.20 mL /cm^2/ day) due to the dissolution of (α-Mg + MgZn) eutectic phases, which reduces microgalvanic corrosion than as-cast one (3.50 ± 0.20 mL /cm^2/ day) [50]. Comparing to as-cast Mg-4Zn alloys, ST Mg-4Zn alloy has a 37% lower hydrogen evolution rate (HER), because the ST treatment decreases the volume fraction of precipitation phases in Mg-4Zn alloys, which reduces the mi-

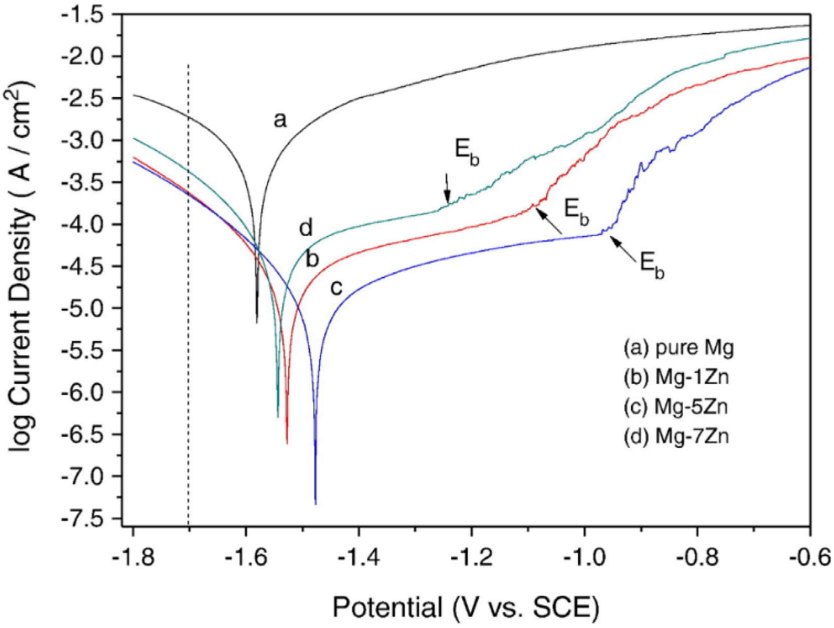

Fig. 7. The potentiodynamic polarization curves of pure Mg and Mg-Zn alloys in SBF. Reprinted from Materials Science and Engineering: C, vol 32, Shuhua Cai, Ting Lei, Nianfeng Li, Fangfang Feng, Effects of Zn on microstructure, mechanical properties and corrosion behavior of Mg–Zn alloys, page no. 2570–2577, Copyright 2012, with permission from Elsevier [41].

Table 5
The list of corrosion data of as-cast various Mg-Zn alloys.

Materials	Electrolyte	E_{corr} (VSC_E)	I_{corr} ($\mu A/cm^2$)	Electrochemical corrosion rate (mm/y)	Immersion corrosion rate (mm/y)	Hydrogen evolution rate ($ml/cm^2/day$)	Ref
Pure Mg	PBS	−1.80	14.6	0.33	–	3.44 (after 11 days)	[43]
Pure Mg	SBF	−1.581	680.1	15.30	34.78 (after 5 days)	–	[41]
Pure Mg	SBF	−1.886	86.06	1.94	–	–	[88]
Pure Mg	HBSS	−1.533	15.98	0.36	–	–	[88]
Mg-0.5Zn	SBF	−1.840	144	2.1	5.19 (after 6 days)		[42]
Mg-1Zn	SBF	−1.527	23.4	0.53	2.01 (after 5 days)	–	[41]
Mg-1Zn	SBF	−1.822	67.30	1.52	–	–	[88]
Mg-1Zn	HBSS	−1.609	10.47	0.24	–	–	[88]
Mg-1Zn	Ringer’s soln.	−1.432	300.18	54.30	162.5 (after 4 days)	213.7 (after 4 days)	[69]
Mg-1.25Zn	SBF	−1.762	282.7	6.45	3.17 (after 6 days)	–	[123]
Mg-1.5Zn	SBF	−1.740	134	1.67	2.91 (after 6 days)		[42]
Mg-2Zn	PBS	−1.75	8.9	0.20	–	3.37 (after 11 days)	[43]
Mg-2.5Zn	SBF	−1.744	242.5	5.54	–	–	[123]
Mg-3Zn	SBF	−1.731	228.3	5.21	1.95 (after 7 days)	–	[53]
Mg-3Zn	SBF	−1.701	103	1.55	1.84 (after 6 days)	–	[42]
Mg-3Zn	SBF	−1.521	12.6	–	–	–	[124]
Mg-3Zn	Ringer’s soln.	−1.621	3.1	0.57	2.03 (after 4 days)	0.65 (after 4 days)	[69]
Mg-4Zn	PBS	−1.73	7.8	0.18	–	2.73 (after 11 days)	[43]
Mg-4Zn	SBF	−1.710	212.4	4.85	2.14 (after 6 days)	–	[123]
Mg-5Zn	SBF	−1.477	11.72	0.26	1.26 (after 5 days)	–	[41]
Mg-5Zn	HBSS	−1.56	33.80	–	–	–	[73]
Mg-5Zn	Ringer’s soln.	−1.591	3.03	0.55	8.04 (after 4 days)	5.02 (after 4 days)	[69]
Mg-6Zn	SBF	−1.759	122	1.83	7.23 (after 6 days)	–	[42]
Mg-6Zn	SBF	−1.759	270.8	6.18	3.48 (after 7 days)	–	[53]
Mg-7Zn	SBF	−1.543	51.79	1.17	3.18 (after 5 days)	–	[41]
Mg-9Zn	SBF	−0.856	147	2.21	11.78 (after 6 days)	–	[42]

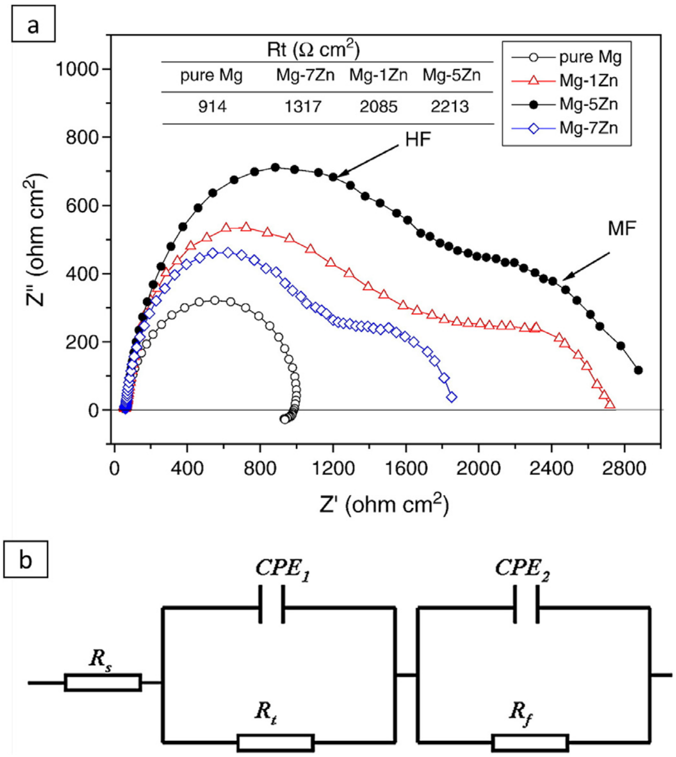

Fig. 8. (a) Nyquist plots for pure Mg and Mg-Zn alloys after soaking in SBF for 1 h and (b) equivalent circuit used for modelling experimental EIS data of Mg-Zn alloys. R_s indicates the corrosive media resistance, R_t indicates the charge transfer resistance, R_f indicates the insoluble layer resistance, CPE_1 indicates the double layer capacitance, and CPE_2 indicates the insoluble salt layer capacitance. Reprinted from Materials Science and Engineering: C, vol 32, Shuhua Cai, Ting Lei, Nianfeng Li, Fangfang Feng, Effects of Zn on microstructure, mechanical properties and corrosion behavior of Mg–Zn alloys, page no. 2570–2577, Copyright 2012, with permission from Elsevier [41].

crogalvanic corrosion, leading to a decreased degradation rate [43]. However, T6 Mg-4Zn alloy has 30% higher HER than as-cast one due to the dispersion of more $MgZn_2$ precipitates mainly at the grain boundaries where the corrosion process preferentially begins and continues from the grain boundaries [43]. The corrosion rate increases monotonically with aging time during T6 treatment, indicating that an increase in aging time leads to an increase in the volume fraction of nano-scale precipitates in Mg-Zn alloy, which results to micro-cathodic effects and increases the degradation rate [50,52]. Similar results were also reported by other researchers [51,52,125]. Table 6 shows the corrosion rate of various heat-treated Mg-Zn alloys in various physiological solutions.

In summary, the heat treatment has significant influence on the corrosion behaviour of Mg-Zn alloy with Zn content of more than 4 wt.%. The T6 treated specimen showed a higher corrosion rate than that of T4 treated one due to the larger volume fraction of Mg_xZn_y secondary phases. Besides, more Mg_xZn_y phases dispersed at the grain boundaries which are preferential site for the corrosion initiation. Therefore, T4 treatment up to 6 h of heat treatment is more preferable to lower the corrosion rate in Mg-Zn alloy as the microstructure did not change after heat treatment beyond 6 h.

4.4. Effect of deformation techniques on the degradation of Mg-Zn alloy

The deformation process leads to much smaller grain sizes, more uniform microstructures, and a lower volume fraction of the precipitates in the deformed samples, which results in a lower degradation rate. Gu et al. observed a lower degradation rate for the hot rolled pure Mg and Mg-1Zn alloy than the corresponding as-cast ones due to the finer grain microstructure [88]. The finer microstructure resulted in a higher density of grain boundaries in the deformed samples compensating the volumetric mismatch in an atomic scale between the Mg matrix and its oxide, making the oxide layer more stable. Additionally, grain boundaries provide excellent nucleation sites for the formation of oxide layer, along with acting as physical corrosion (diffusion) barriers against corrosion propagation. Furthermore, an increase in the rolling cycle resulted in an increased degradation rate for Mg-3Zn alloy [55]. Zou et al. observed uniform corrosion with small depth pits for the HSRR Mg-4Zn sample in 0.9% NaCl, whereas the interconnected deeper pits with non-uniform corrosion for the as-cast sample [56]. Similarly, Mg-4Zn samples deformed by MDF or extrusion showed decreased degradation rates by 63% and 74% respectively than that of the as-cast one [43]. The higher degradation rate in the MDF-processed sample than the extruded one is attributed to the inhomogeneous microstructure consisting of some un-recrystallized grains with high dislocation density and high energy together with some low-energy DRXed grains in the MDF specimen. The recrystallized grains act as anode and the un-recrystallized grains as cathodic sites, resulting in microgalvanic corrosion. Therefore, the density of dislocations can influence the corrosion behaviour of the material. Generally, the regions with a higher dislocation density act as anode, whereas those with a lower dislocation density act as cathode. This might result in the microgalvanic effect increasing the corrosion rates in Mg alloys [126]. MDF-processed Mg-6Zn alloy has decreased cathodic kinetics and growth of oxide layer along with refined microstructure, which resulted in a lower degradation rate than the homogenised sample [84]. Furthermore, the electrode reaction kinetics of the alloy decreased with the increase in the total length of the grain boundaries [127]. Similarly, a reduced degradation rate with uniform corrosion was also observed after FSPed [65] and Hot Extrusion + ECAP-stimulated solution treatment [77] of Mg-Zn samples. However, an increased degradation rate for the Mg-Zn specimen was observed after some deformation process such as on ECAP-BP [62], and tensile and compressive deformation [72]. The increase in degradation rate by some deformation process may be attributed to accumulation of structural defects (*e.g.* dislocations and deformation twins), increased residual stress, which leads to the enhancement of intergranular corrosion and stress corrosion. Table 7 shows the corrosion rate of various deformed Mg-Zn alloys in various physiological solutions. Fig. 9 indicates the corrosion rates of Mg-Zn alloys in simulated body fluids, revealing that Mg-5 wt.% Zn alloys showed the lowest degradation rate among other as-cast alloys.

Table 6
The list of corrosion data of various heat-treated Mg-Zn alloys.

Materials	Processing methods	Medium	E_{corr} (VSC_E)	I_{corr} ($\mu A/cm^2$)	Electro-chemical corrosion rate (mm/y)	Immersion corrosion rate (mm/y)	Hydrogen evolution rate ($ml/cm^2/day$)	Ref
Mg-3Zn	T4 for 6 h	SBF	−1.730	223.6	5.10	1.92 (after 7 days)	–	[53]
Mg-3Zn	T4 for 12 h	SBF	−1.724	216.2	4.94	1.87 (after 7 days)	–	[53]
Mg-3Zn	T4 for 18 h	SBF	−1.718	210.7	4.81	1.85 (after 7 days)	–	[53]
Mg-4Zn	ST	PBS	−1.71	5.8	0.13	–	1.71 (after 11 days)	[43]
Mg-4Zn	T6	PBS	−1.69	50.0	1.14	–	3.54 (after 11 days)	[43]
Mg-6Zn	T4 for 6 h	SBF	−1.702	205.2	4.68	1.42 (after 7 days)	–	[53]
Mg-6Zn	T4 for 12 h	SBF	−1.692	198.4	4.53	1.38 (after 7 days)	–	[53]
Mg-6Zn	T4 for 18 h	SBF	−1.682	191.5	4.37	1.36 (after 7 days)	–	[53]

Table 7
The list of corrosion data of various deformed Mg-Zn alloys.

Materials	Processing methods	Medium	E_{corr} (VSC_E)	I_{corr} ($\mu A/cm^2$)	Electro-chemical corrosion rate (mm/y)	Immersion corrosion rate (mm/y)	Hydrogen evolution rate ($ml/cm^2/day$)	Ref
Pure Mg	Hot Rolled at 400 °C	SBF	−1.796	37.24	0.84	–	–	[88]
Pure Mg	Hot Rolled at 400 °C	HBSS	−1.544	9.58	0.22	–	–	[88]
Mg-1Zn	Hot Rolled at 400 °C	SBF	−1.805	40.78	0.92	–	–	[88]
Mg-1Zn	Hot Rolled at 400 °C	HBSS	−1.549	7.55	0.17	–	–	[88]
Mg-4Zn	MDF	PBS	−1.65	2.6	0.06	–	1.02 (after 11 days)	[43]
Mg-4Zn	Extruded	PBS	−1.53	1.2	0.03	–	0.72 (after 11 days)	[43]
Mg-4Zn	Extruded	PBS	−1.65 ± 0.03	60.3 ± 3.3	1.37 ± 0.07	–	–	[76]
Mg-6Zn	Extruded	SBF	−1.62	45.0	–	~0.07 (after 30 days)	–	[121]
Mg-6Zn	Hot extruded at 250 °C	SBF	−1.56	–	0.16	0.07 ± 0.02 (after 30 days)	–	[57]

4.5. Effect of surface treatment on the degradation of Mg-Zn alloy

Several researchers further employed different surface treatment techniques to control the degradation rate of Mg-Zn alloy by postponing the start of the degradation process [132]. The coated Mg-Zn alloy showed a lower corrosion rate as compared to the uncoated one because the coating surface hinders the transport of ions. The corrosion resistance increases with an increase in the thickness of the coating layer. In some cases, the decreased corrosion resistance with thicker coatings as compared to the thinner coatings is due to the presence of defects such as pores and microcracks on the coating surface. The heat treatment performed after coating consolidates the coating layer and thereby further increases the corrosion resistance.

For Mg-Zn alloys for biomedical application, the coating material can be divided into bioinert or bioactive coating [133]. The bioactive coating is more preferable as it helps an implant to mimic the natural properties of organ. For bone tissue application, various form of Ca-P coating such as brushite (DCPD) [134,135], hydroxyapatite (HA) [68,134] [136], and fluoridated hydroxyapatite (FHA) [134] were explored to reduce the degradation rate in Mg-Zn alloy. In addition to controlling the degradation rate, the Ca-P coating also helps in healing of bone tissue. The FHA-coated Mg-6Zn alloy offers long-term stability and corrosion resistance than DCPD and HA coating due to its largest stack density, the lowest solubility products and a closely packed organization [134]. Furthermore, more biomineralization behaviour of FHA-coated Mg-Zn alloy was observed due to the appearance of more and better crystallized Ca-P formation on the interface of biomaterials [137] The carbonate apatite (CAp) coated Mg-Zn specimen also showed lower corrosion rate than HA-coated one, indicating the more corrosion resistance behaviour of CAp-coating [138]. Researchers also performed MAO coatings [139] and $MgCO_3 \cdot 3H_2O$ (nesquehonite) coating [128] on Mg-Zn alloy, improving corrosion resistance in coated ones. Recently, researchers employed double-layer coating and composite coatings such as nicotinic acid pretreatment (NA)/calcium phosphate composite coating [124], Ca-P/chitosan coating [140], and HA coating on MAO-treated [141] Mg-Zn alloys to improve the surface properties and enhanced the corrosion resistance of the alloys. Furthermore, a combination of both deformation and coating techniques such as extrusion + hydrothermal coating showed a lower corrosion rate for the Mg-4Zn alloy than the extruded Mg-4Zn alloy [76].

5. Evaluation of biological safety and functionality

5.1. Basic principle of biological safety evaluation

The biocompatibility of metallic materials depends on its stability in the biological environment. It can be evaluated at different levels including cellular, tissue, and human/clinical-related biocompatibility [1]. Metal ions and wear debris released by implant degradation may influence the biological functions of cells and tissue adjacent to implanted materials. In the case of a biodegradable metal, its corrosion rate inside the human body will strongly influence its biological safety. Therefore, recreation of the corrosion environment in the implanted site is the key issue for its biological safety evaluation.

5.2. In vitro *cell culture studies of Mg-Zn alloy*

Cytotoxicity test is incorporated as the basic evaluation of the biological safety of chemicals since the correlation between cytotoxicity and human acute toxicity is confirmed [142]. In the case of implant materials' evaluation, cytotoxicity correlates to the thickness of the fibrous tissue formed around the implant materials, which is the parameter for the inflammation level induced by implantation [142,143]. ISO 10993–5 offers a basic procedure for cytotoxicity evaluation of biomaterials, indicating to use of established cell lines such as L929 (NCTC clone 929), Balb/3T3, MRC-5, WI-38, Vero, BHK-21 and V-79. It also indicates the two methods for cytotoxicity testing; a direct contact method and an extract method. In the extract method, extract condition is crucial to obtain reasonable results for a biodegradable metal.

Like ISO 10993–5, the most of cytotoxicity tests employ cellular proliferation or viability as their endpoints. Beyond these kinds of tests, materials' effects on cellular function such as specific biomolecule synthesis, mineral nodule formation, and messenger RNA expression are also investigated using *in vitro* cell culture technique. These kinds of cytocompatibility tests become popular in recent years but it should be noticed that their relevance to *in vivo* or clinical implantation results is unproved. Similarly, primary cells are frequently employed to cytocompatibility tests since establish cell lines often reported their loss in some cellular function which is observed by *in vivo* experiments. However, availability of primary cells is limited, resulting in uncertain reproducibility and reliability of their results. This is the reason that ISO 10993–5 recommends to use the well-established cell lines for their high reproducibility and reliability on their results.

Tables 8 indicates the results of cytotoxicity and cytocompatibility evaluation of Mg-Zn alloys. The results for Mg-Zn specimens with surface treatment are also summarized in Table 9. Regarding the uncoated Mg-Zn alloys, the results of the extract method gave no significant cytotoxicity comparing to those without the extract solution either as-cast nor deformed samples. However, by the direct method, extruded Mg-6Zn alloy specimen suppresses the adhesion and spreading of murine calvarial osteoblastic cells MC3T3-E1 in comparison to PLLA [121]. Therefore, surface coating is effective to improve cell viability on direct contact to Mg-Zn alloy surface [136,138,139,144]. HA-coated Mg-3Zn alloy surface gave 41% higher cell viability of MG-63 (human osteosarcoma-derived cells) than the uncoated one at days 1 and 3 [136]. However, the cell viability decreases after day 3 than day 1, indicating the influence of substrate corrosion [136]. In addition to cytotoxicity of FHA-coated Mg-6Zn alloy by direct contact, Li et al. confirmed the higher osteoblastic differentiation and activity on the coated surface using human bone marrow stromal cells (hBMSCs) [144]. This result agrees with that Mg^{2+} stimulates the osteogenesis [145]. The osteogenic activity of the Mg-Zn alloy can be partly ascribed to the Zn^{2+}, which can stimulate bone formation and increase osteogenic function in osteoblasts by stimulating cell proliferation, alkaline phosphatase activity, collagen synthesis, and osteoblast marker gene expression [146].

5.3. Antibacterial effect of Mg-Zn alloy

The implants possessing antibacterial behaviour are more desirable for better clinical performance as they reduce the risk of implant-associated infection. ISO 22196 offers the basic protocols for the evaluation of the antibacterial activity of plastics and non-porous surfaces. The contact condition is crucial for evaluating the antibacterial activity of biodegradable metals [150]. The antibacterial activity of the Mg-Zn alloy was possibly attributed to the synergistic effects of high alkalinity and released Zn^{2+} due to its degradation process [147]. The high alkalinity ($pH \geq 9$) decreases the bacterial surface hydrophobicity [151] and prevented biofilm formation on Mg surface [152]. Bacterial adhesion and growth can be inhibited by reactive oxygen species (ROS) generated by ZnO [153], and Zn^{2+} are able to inhibit transmembrane proton translocation, glycolysis, and acid tolerance in bacteria [154]. Therefore, ZnO on the surface of the Mg-Zn alloy and Zn^{2+} released by the degradation of the Mg-Zn alloy may contribute to enhancing its antibacterial properties.

5.4. Blood compatibility of Mg-Zn alloy

The blood compatibility plays a determined role in the clinical applications as the implant inevitably come in contact with blood during implantation. When the implant comes into contact with blood, plasma protein adsorption occurs within a very short time, and the adsorbed plasma protein plays a major role in the blood reactions (including platelet activation, hemolytic reaction, and coagulation factor activation, etc.) [155,156]. ISO 10993–4:2002 offers the basic protocols for the evaluation of the blood compatibility for medical devices. Extruded Mg-6Zn alloy showed a hemolysis rate of 3.4%, which is less than 5%, indicating the non-destructive

Table 8
The results in cytocompatibility evaluation of Mg-Zn alloys.

Materials	Processing	Methods[a]	Cells	Inoculated number	Incubation period	End point	Control	Results	Ref
Mg-1Zn	As-cast	Extract	L929 NIH3T3 MC3T3-E1 ECV304 VSMC	5×10^3 in 100 μL	2, 4, and 7 days	Viability	Pure Mg	No cytotoxicity with enhanced cell viability than pure Mg.	[88]
Mg-5.6Zn	As-cast	Extract	Rat BMSC	3×10^3 per 96 well 1×10^5 per 6 well	1, 3, and 5 days 2 and 3 weeks 4, 7, and 10 days 7 and 14 days	Viability Calcification ALP RT-PCR	Ti	(i) Similar cell viability to control. (ii) More mineralized nodules and higher ALP activity for Mg-Zn extract than control. (iii) Increased expression of differentiation markers for Mg-Zn extract at day 7 but no difference at day 14.	[147]
Mg-6Zn	Extrusion	Direct	MC3T3-E1	1×10^4 per 24 well (0.5~1 mL)	2 h	Adhesion (morphology)	PLLA	Mg-6Zn is able to support earlier adhesion of cells, but they do not spread as sufficiently as those on PLLA.	[121]
Mg-5.6Zn	Extrusion	Direct	MC3T3-E1	1×10^5/cm^2 (in 24 well) 1×10^5/well	1, 2, 4h 21 days Every 3 days	Attachment Mineralization RT-PCR	PLLA	(i) More cells attached to Mg-Zn alloy than PLLA. (ii) Greater area of mineralized nodules formed on Mg-Zn alloy than PLLA. (iii) collagen (COL) 1α1 and osteocalcin (OC) mRNA were at a higher level for Mg-Zn group than PLLA at day 3 and 12, respectively.	[148]
Mg-6Zn	Extrusion	Extract	L929	2.5×10^3 in 100 μL	2, 4, and 7 days	Relative growth rate (RGR)	No sample	No significant difference in RGR between the extracts and negative control.	[57]
Mg-6Zn	Extrusion + aging at 150 °C for 24h	Extract	L929	not mentioned	1, 4, and 7 days	Relative growth rate (RGR)	No sample	No significant difference in RGR between the extracts and negative control.	[61]

[a] The method how the cells contact to the testing sample; the extract method employs extract solution added into culture medium, and in the direct method, cells are directly inoculated onto the material surface and cultured on it.VSMC, vascular smooth muscle cells. BMSC: bone mesenchymal stem cell.

Table 9
The list of cytocompatibility evaluation of surface-coated Mg-Zn alloys.

Materials	Surface modification	Methods[a]	Cells	Inoculated number	Incubation period	End point	Control	Results	Ref
Mg-1Zn Mg-5Zn Mg-7Zn	CAp-coated HA-coated	Direct	MC3T3-E1	$2 \times 10^{4}/\mathrm{cm}^{2}$ (in 2 mL)	3 days	Viability	Uncoated sample	CAp and HA coatings enhanced the cell viability on the Mg-Zn alloys, but the Cap coatings improved it more effectively than the HA coating.	[138]
Mg-3Zn	HA-coated	Direct (after pre-incubation in SBF or D-MEM)	MG-63	5×10^{4} / 50 μL	4 h 1, and 3 days	Adhesion, viability and morphology	Uncoated alloy and TCPS	(i) Coated sample had better initial cell adhesion even than TCPS. (ii) The coated ones had 41% higher cell viability than the uncoated ones at days 1 and 3, but the cell viability at day 3 decreased than day 1 and TCPS.	[136]
Mg-6Zn	FHA-coated	Direct	hBMSC	1×10^{4}/disc 5×10^{3}/disc 5×10^{3}/disc 2×10^{4}/disc	24h 1–4 days 7, 14, 21 days 7, 14, 21 days	Morphology Viability ALP RT-PCR	Uncoated Mg-6Zn	(i) Cells on both uncoated and coated samples spread well. (ii) Higher proliferation observed on coated ones at days 2 and 3. (iii) Higher ALP levels appeared on coated ones at days 14 and 21. (iv) The up-regulation was suggested on coated ones after 21 days of culture.	[144]
Mg-6Zn	FHA-coated	Extract	hBMSC	5×10^{3} per 96 well	2, 4, and 7 days	Viability and morphology	No sample	(i) No significant difference in cell viability at days 2 and 4, but the higher viability on the extracts than the negative control at day 7. (ii) No morphological change was observed in 100% extract.	[149]
Mg-6Zn	MAO-coated	Direct	Rabbit BMSC	$5 \times 10^{4}/\mathrm{cm}^{2}$	6, 12, and 24 h	Adhesion	Uncoated sample	(i) Coated samples showed improved the cell viability, cell adhesion and spreading. (ii) ALP activity is enhanced with increase in extract concentration of coated samples. (iii) Col-I expression increased on both uncoated and coated samples.	[139]
		Extract		1×10^{3}/100 μL	1, 3, and 5 days	Viability			
				1×10^{4}/mL	14 days	ALP Col-I			

[a] In the extract method, extract solution of the testing materials was added into culture medium. In the direct method, cells are inoculated onto the testing material.FHA, Fluoridated Hydroxyapatite; HA, Hydroxyapatite; CAp, carbonate apatite; MAO, Microarc Oxidation; TCPS, tissue culture polystyrene; ALP, alkaline phosphatase activity assay; RT-PCR, Reverse transcription-polymerase chain reaction assay; hBMSC, human bone marrow-derived stem cell.

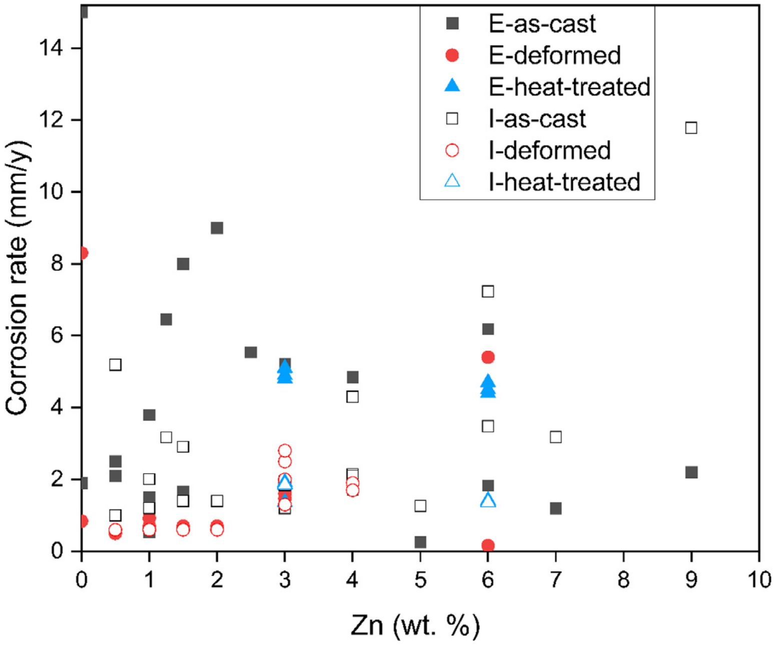

Fig. 9. The corrosion rate of various Mg-Zn alloys after the electrochemical test and immersion test in SBF. E and I indicate electrochemical and immersion tests, respectively. The data sources are following references: E-as-cast from [41,42,44,53,85,88,123,128], E-deformed from [44,55,57,88,129], E-heat-treated from [53], I-as-cast from [41,42,44,53,55,123,130], I-deformed from [44,55,131], and I-heat-treated from [53].

effect on red blood cells (RBCs) [121]. However, pure Mg has a high hemolysis rate of 59.24% because of its higher degradation rate [157]. The larger increase in local pH accompanying to higher degradation rate of pure Mg promotes the binding between hemoglobin and cellular membrane and enhances the uptake of Ca^{2+} by RBCs, resulting in the rupture of RBCs leading to hemolysis. Zn^{2+} are reported to reduce the fragility of RBCs and to maintain the enzyme activities, which is contributing to reduction in hemolysis [158,159]. Furthermore, the less corrosion of Mg-Zn alloys and the anticoagulant properties of Zn^{2+} may contribute to less platelet adhesion and activation, that means better anticoagulant performance [160]. Therefore, the alloying of Mg with Zn may lead to better blood compatibility. The surface treatment such as MAO coating on Mg-6Zn alloy further improved the blood compatibility by reducing the hemolysis rate from 4 (without coating) to 1.9% [139], suggesting the further reduction of corrosion reaction and resulting local pH shift is preferable for the devices contacting to blood for long period of time.

5.5. *In vivo implantation studies of Mg-Zn alloy*

In vivo implantation is a widely used method to estimate the biological performance and safety of a biomedical device due to the assumption of nearly similar physiological conditions in the testing animals and humans. Regarding the Mg-Zn alloys, only one alloy, Mg-5.6Zn was extensively studied by the group of Shanghai Jiaotong University and Shanghai Sixth People's Hospital.

Implantation of a Mg-5.6Zn rod into the distal femur marrow cavity of the New Zealand rabbit resulted in the material degradation of 87% after 14 weeks with no measurable influence in serum magnesium, or on liver and kidney functions [57,161]. The serum uric acid and creatine kinase increased transiently after the surgery but returned to preoperative levels 1 weeks after the surgery [161]. There were no changes in the histology of the heart, liver, kidney, or spleen postoperatively [161]. These observations suggest that Mg-Zn alloy has good biocompatibility with no damages on vital organs by femur implantation.

The degradation behaviour of the implanted Mg-5.6Zn rod was confirmed radiographically; the macroscopic degradation starts in the first 3 weeks after post-implantation with the evidence of fuzzy implant edges accompanied by subcutaneous bubbles (Fig. 10a), and gradual progress in degradation was indicated by too blurry radiograph of the implant (Fig. 10b) at 12 weeks after post-implantation [57,161] After 3 weeks, the tissues around the gas bubble are composed of two layers, an inner compact one and an outer loose connective tissue (as shown in Fig. 11) [57]. No adverse effects due to these gas bubbles were observed and they disappeared after 6 weeks without any intervention [57,161], indicating the diffusion of hydrogen gas into the surrounding tissues.

Observation of the cross-sections of the implanted rods after 12 weeks of post-implantation also confirmed the marked degradation of Mg-5.6Zn rod with the irregular shapes accompanied by the layer of degradation products and newly formed bone [148]. Neither inflammation nor fibrous membrane was presented at the interface between the Mg-5.6Zn rods and the bone tissue, whereas continuous fibrous membranes were formed for PLLA rods [148]. Furthermore, in comparison to Ti Kirschner wires, Mg-5.6Zn rods had more new bone formation and enhanced bone-to-implant contact around the implants after 8 weeks of post-implantation into the distal femur

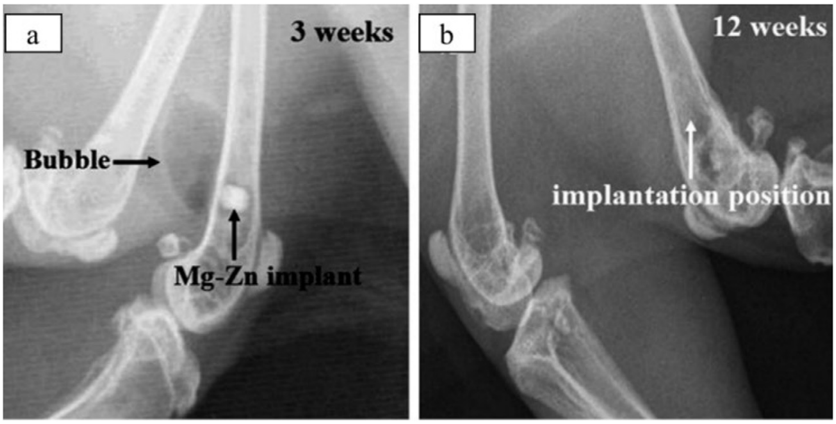

Fig. 10. Radiographs of hot extruded Mg-5.6Zn rod at 3 weeks (a) and 12 weeks (b) post-implantation. Reprinted from Acta Biomaterialia, vol 6, Issue 2, Shaoxiang Zhang, Xiaonong Zhang, Changli Zhao, Jianan Li, Yang Song, Chaoying Xie, Hairong Tao, Yan Zhang, Yaohua He, Yao Jiang, Yujun Bian, Research on an Mg–Zn alloy as a degradable biomaterial, page no. 626–640, Copyright 2010, with permission from Elsevier [57].

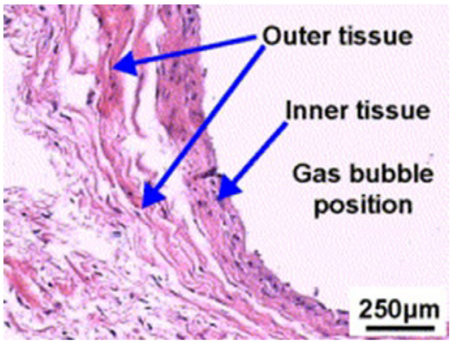

Fig. 11. Hematoxylin and eosin (HE) stained tissues around the gas bubble at 3 weeks post-implantation. Reprinted from Acta Biomaterialia, vol 6, Issue 2, Shaoxiang Zhang, Xiaonong Zhang, Changli Zhao, Jianan Li, Yang Song, Chaoying Xie, Hairong Tao, Yan Zhang, Yaohua He, Yao Jiang, Yujun Bian, Research on an Mg–Zn alloy as a degradable biomaterial, page no. 626–640, Copyright 2010, with permission from Elsevier [57].

of the rat [147]. Mg-5.6Zn pin had better healing with reduced inflammation than Ti pin after 4 weeks of post-implantation into the cecum of the Sprague-Dawley rats [162]. At this implantation site, no emphysema was formed due to the rapid adsorption of hydrogen gas by the intestine [147].

Implantation of an extruded Mg-5.6Zn tube into the common bile duct (CBD) of adult New Zealand rabbits confirmed the majority of the Mg-5.6Zn tube remained in the CBD after 1-week post-implantation, whereas 91% of the tube degraded after 3 weeks of post-implantation [163]. These data indicate that the degradation rate of the implant depends on the implantation site.

To suppress the quick degradation and improve the interface bioactivity of the implant, FHA coating was applied to Mg-5.6Zn alloy [149]. Implantation into the femoral shaft of adult New Zealand rabbits confirmed more direct contact on FHA-coated alloy than uncoated one after 1 month post implantation [149]. From the above literature, it can be concluded that Mg-5.6Zn alloy degraded in a controlled manner accompanied by new bone formation with enhanced bone-to-implant contact (Table 10). The released Mg^{2+} and Zn^{2+} during the degradation of Mg-5.6Zn alloy may help the formation of new bone near the implant site. The degradation rate of the implant also depends on the implantation site. However, the implantation condition into the animal body differs from that into human body in terms of size, body weight, amount of body fluid, etc. which sometimes leads to undesired results even though they had good compatibility by *in vivo* implantation tests.

6. Future areas and challenges

This section addresses the difficulties that the researchers have encountered in the studies of biodegradable Mg-Zn alloys and the topics that require additional focus in this field. In the future, the combination of thermo-mechanical deformation and surface modification techniques could attract attention. As described Section 3, the highest UTS of Mg-Zn alloy is 301 MPa with 4 wt.% Zn, which is lower than that of Ti grade 2, which is employed for conventional nondegradable microplates and screws as temporary implants. The application of the material with lower mechanical properties brings the increase in the device thickness, which is generally unwelcome due to the spatial limitation in the tissue for the bone fixture implant. Therefore, deformation techniques are primarily utilized to increase mechanical properties, which is the basic requirement for the application to temporary bone fixture devices. The effect of different processing techniques on the degradation behaviour and following antibacterial activity of Mg-Zn alloy also needs attention.

The surface modification is mandatory to avoid the early degradation of the implant, which causes the formation of gas cavity in surrounding tissue, resulting in retardation of healing process. In one of the *in vivo* implantation studies introduced in Section 5.4, the tunnel of the rabbit femur made by sham operation in control group healed within 3 weeks, but in the Mg-5.6Zn implant group, the large gaps between the implant and bone tissue were observed even after 14 weeks

Table 10
The list of results from the *in vivo* test of Mg-Zn alloys.

Materials	Processing	Animal	Implantation site	Implantation period	Control material	Results	Ref
Mg-5.6Zn	Extruded	Rabbit	Femoral marrow cavity	18 weeks	Without implant	(i)New bone formation with 87% of implant material degradation (ii)The gas bubbles were disappeared after 6 weeks of post implantation indicating the diffusion of hydrogen gas into the surrounding tissues	[57]
Mg-5.6Zn	(Extruded)	Rabbit	Femoral marrow cavity	14 weeks	Without implant	Mg-Zn alloy is resorbable (degraded 87%) when implanted in bone. It has no effect on the chromaticness, structure or function of heart, liver, kidney, or spleen.	[161]
Mg-5.6Zn	(Extruded)	Rabbit	Femoral marrow cavity	12 weeks	Poly-L-lactic acid (PLLA)	(i)The Mg-5.6Zn alloy not only degraded faster but was accompanied by more new bone formation than PLLA (ii) The fibrous membrane was observed only at interface between bone tissue and PLLA implant	[148]
Mg-5.6Zn	(Extruded)	Rat	Femoral marrow cavity	8 weeks	Ti Kirschner wire	More new bone formation and enhanced bone-to-implant contact were observed around the Mg-Zn alloy implants than around the Ti implants	[147]
Mg-5.6Zn	Extruded	Rabbit	Common bile duct (CBD)	3 weeks	Stainless steel	After 1 week most of the stent structure retained whereas after 3 weeks 91% of Mg-5.6Zn stent degraded	[163]
Mg-5.6Zn	Extruded	Rat	Cecum	4 weeks	Ti	(i)Better healing and reduced inflammation for Mg-6Zn than Ti (ii)H_2 gas was rapidly absorbed by the intestine and not formed emphysema in the implantation site	[162]
Mg-5.6Zn	FHA coated	Rabbit	Femoral condyle	4 weeks	–	FHA coating enhance the interface bioactivity mainly by inducing quicker differentiation and decreasing the degradation rate to make a better contacted interface	[149]

of implantation [161]. To improve this, FHA-coating was employed and succeeded to have direct contact between the implant and bone tissue at 1-month post-operation [149]. More techniques will be studied for the control of implant degradation rate and interfacial activity. Research on the composite coating layers is one of them, where the inner layer reduces the rate of substrate corrosion and the outer layer delays the onset of the corrosion process. A thorough investigation into the impact of different ceramic-polymer coating combinations on the corrosion process is also necessary.

The human interstitial fluid contains inorganic ions as well as organic components such as amino acids, lipids, carbohydrates, and proteins. Its pH is influenced by the gas composition inside the body; 5% CO_2, 5% O_2, and 90% N_2 in peripheral tissue. Blood flow supplies nutrition and oxygen to every tissue via capillary network, which also helps diffusion of metabolites and waste molecules. The fluid composition, gas partial pressure, and diffusion rate by circulation differ with implanting tissue and organ. Therefore, more research is still needed to analyse the mechanical and corrosion properties of the Mg-Zn alloy in the intricate human physiological environment.

Even though a few *in vivo* studies on Mg-Zn alloys have been conducted, more thorough *in vivo* investigations are necessary prior to conducting clinical trials. The mechanism of hydrogen absorption and whether the hydrogen can be metabolized or will accumulate in certain organs are still unknown and need further detailed investigation. Furthermore, the results of animal studies not always give the same results to those in human clinical cases. The recreation of pathological condition is a critical issue to lead the success of device development in an efficient manner. Not only an *in vivo* model but also *in vitro* experimental techniques including tissue engineering should be investigated for better understanding of the requirements for the implant device treating a specific injury or diseases.

7. Conclusions

An ideal biodegradable material should possess sufficient mechanical properties, a degradation rate aligning with the tissue healing process, and excellent biocompatibility. In the case of Mg-Zn alloy, the degradation rate decreases with the addition of up to 5 wt.% Zn, achieved through the formation of ZnO, which is more stable than MgO in aquas condition. However, further additions lead to an increased degradation rate due to the formation of a more continuous network-like structure of the secondary phase, leading to localized corrosion. Similarly, mechanical properties exhibit significant improvement up to 4 wt.% Zn, beyond which no notable enhancement is observed due to the formation of a network structure with dendritic segregation along grain boundaries caused by a higher number of second phases. Therefore, the optimal composition for implant applications is identified as Mg-Zn alloy with 4.0-5.0 wt.% Zn.

Various thermo-mechanical processing techniques can enhance mechanical properties and corrosion resistance, but optimization of processing parameters is crucial. Decreasing grain size and reducing the secondary phase through suitable deformation processes improve mechanical properties and increase corrosion resistance. The decreased grain size enhanced surface homogeneity, while a lower amount of secondary phase results in a discontinuous distribution, reducing the degradation rate. However, in some cases, lower grain size post-deformation may not decrease the degradation rate due to the presence of high dislocation densities.

Coating Mg-Zn alloy reduces corrosion rate by hindering ion transport. Mg-Zn alloys processed by suitable techniques such as deformation and proper surface treatment showed better cell adhesion and proliferation, and excellent biocompatibility compared to the as-cast alloy. The Mg^{2+} produced as a result of *in vivo* degradation help in the formation of new bone near the implant site. The presence of Zn in the Mg-Zn alloy may contribute to strengthen the bone-implant contact region.

In conclusion, biodegradable Mg-Zn alloys show promise as potential candidates for temporary implant applications. With further development, they are anticipated to partially replace traditional metallic implants and serve as next-generation implants.

Declaration of competing Interest

The authors declare that they have no known competing financial interests or personal relationships that could have appeared to influence the work reported in this paper.

CRediT authorship contribution statement

Manas Ranjan Sahu: Writing – review & editing, Writing – original draft, Visualization, Validation, Software, Methodology, Investigation, Conceptualization. **Akiko Yamamoto:** Writing – review & editing, Writing – original draft, Supervision, Resources, Methodology, Funding acquisition, Conceptualization.

Data availability

Data will be available on request.

References

[1] Y. Liu, et al., Adv Funct Mater 29 (18) (2019), doi:10.1002/adfm.201805402.
[2] J. Venezuela, M.S. Dargusch, Curr Opin Solid State Mater Sci 24 (3) (2020) 100822, doi:10.1016/j.cossms.2020.100822.
[3] C. Shuai, S. Li, S. Peng, P. Feng, Y. Lai, C. Gao, Mater Chem Front 3 (4) (2019) 544–562, doi:10.1039/C8QM00507A.
[4] A. Francis, Y. Yang, S. Virtanen, A.R. Boccaccini, J Mater Sci Mater Med 26 (3) (2015) 138, doi:10.1007/s10856-015-5473-8.
[5] J. Venezuela, M.S. Dargusch, Acta Biomater 87 (2019) 1–40, doi:10.1016/j.actbio.2019.01.035.
[6] A.R. Khan, N.S. Grewal, C. Zhou, K. Yuan, H.-J. Zhang, Z. Jun, Res Engineering 20 (2023) 101526, doi:10.1016/j.rineng.2023.101526.
[7] F. Gao, et al., Corros Sci 240 (2024) 112439, doi:10.1016/j.corsci.2024.112439.
[8] M.R. Sahu, T.S.S. Kumar, U. Chakkingal, J Magnes Alloys 10 (8) (2022) 2094–2117, doi:10.1016/j.jma.2022.08.002.
[9] A. Dehghanghadikolaei, H. Ibrahim, A. Amerinatanzi, M. Elahinia, Biodegradable Magnesium Alloys, 2nd ed., Elsevier Ltd., 2019, doi:10.1016/b978-0-08-102666-3.00009-2.
[10] C. Pan, et al., J Magnes Alloys 11 (1) (2023) 48–77, doi:10.1016/j.jma.2022.12.017.
[11] Y. Lu, S. Deshmukh, I. Jones, Y.-L. Chiu, Biomater Transl 2 (3) (2021) 214–235, doi:10.12336/biomatertransl.2021.03.005.
[12] Y. Yamasaki, et al., Biomaterials 24 (27) (2003) 4913–4920, doi:10.1016/S0142-9612(03)00414-9.
[13] V. Tsakiris, C. Tardei, F.M. Clicinschi, J Magnes Alloys 9 (6) (2021) 1884–1905, doi:10.1016/j.jma.2021.06.024.
[14] Y.F. Zheng, X.N. Gu, F. Witte, Mater Sci Engineering R: Reports 77 (2014) 1–34, doi:10.1016/j.mser.2014.01.001.
[15] M. He, L. Chen, M. Yin, S. Xu, Z. Liang, Journal of Mater Res Technol 23 (2023) 4396–4419, doi:10.1016/j.jmrt.2023.02.037.
[16] D. Liu, D. Yang, X. Li, S. Hu, J Mater Res Technol 8 (1) (2019) 1538–1549, doi:10.1016/j.jmrt.2018.08.003.
[17] M. Hashemi, R. Alizadeh, T.G. Langdon, J Magn Alloys 11 (7) (2023) 2260–2284, doi:10.1016/j.jma.2023.07.009.
[18] M. Sabbaghian, R. Mahmudi, K.S. Shin, J Magnes Alloys 7 (4) (2019) 707–716, doi:10.1016/j.jma.2019.11.001.
[19] Y. Chen, S. Zhang, J. Li, Y. Song, C. Zhao, X. Zhang, Mater Lett 64 (18) (2010) 1996–1999, doi:10.1016/j.matlet.2010.06.011.
[20] Y. Zhang, J. Li, J. Li, J Alloys Compd 728 (2017) 37–46, doi:10.1016/j.jallcom.2017.08.264.
[21] H. Li, Q. Peng, X. Li, K. Li, Z. Han, D. Fang, Mater Des 58 (2014) 43–51, doi:10.1016/j.matdes.2014.01.031.
[22] K. Szentmihályi, P. Vinkler, J. Fodor, J. Balla, B. Lakatos, Orv Hetil 150 (15) (2009) 681–687, doi:10.1556/oh.2009.28591.
[23] A. Bandyopadhyay, I. Mitra, S.B. Goodman, M. Kumar, S. Bose, Prog Mater Sci 133 (2023) 101053, doi:10.1016/j.pmatsci.2022.101053.
[24] K. Prasad, et al., Materials (Basel) 10 (8) (2017) 884, doi:10.3390/ma10080884.
[25] H. Breme, J. Helsen, Metals As Biomaterials, 1998, pp. 1–35.
[26] T. Hanawa, in: Metallic Biomaterials Metals For Medical devices, CRC Press, Boca Raton, 2024, pp. 148–179, doi:10.1201/9781003357827.
[27] R. Osman, M. Swain, Materials (Basel) 8 (3) (2015) 932–958, doi:10.3390/ma8030932.
[28] T. Hanawa, in: Metallic Biomaterials Metals For Medical devices, CRC Press, Boca Raton, 2024, pp. 180–192, doi:10.1201/9781003357827.
[29] K. Van de Velde, P. Kiekens, Polym Test 21 (4) (2002) 433–442, doi:10.1016/S0142-9418(01)00107-6.
[30] S.C. Cifuentes, et al., Mater Lett 74 (2012) 239–242, doi:10.1016/j.matlet.2012.01.134.
[31] N. Eawwiboonthanakit, M. Jaafar, Z.A.A. Hamid, M. Todo, B. Lila, Adv Mat Res 1024 (2014) 179–183, doi:10.4028/www.scientific.net/AMR.1024.179.
[32] G. Gąsior, J. Szczepański, A. Radtke, Materials (Basel) 14 (12) (2021) 3381, doi:10.3390/ma14123381.
[33] C.C. Ng, M.M. Savalani, M.L. Lau, H.C. Man, Appl Surf Sci 257 (17) (2011) 7447–7454, doi:10.1016/j.apsusc.2011.03.004.
[34] Y. Zhou, et al., J Alloys Compd 687 (2016) 109–114, doi:10.1016/j.jallcom.2016.06.068.
[35] M.P. Staiger, A.M. Pietak, J. Huadmai, G. Dias, Biomaterials 27 (9) (2006) 1728–1734, doi:10.1016/j.biomaterials.2005.10.003.
[36] P. Wen, et al., Mater Des 155 (2018) 36–45, doi:10.1016/j.matdes.2018.05.057.
[37] B. Song, S. Dong, S. Deng, H. Liao, C. Coddet, Opt Laser Technol 56 (2014) 451–460, doi:10.1016/j.optlastec.2013.09.017.
[38] B. Song, S. Dong, Q. Liu, H. Liao, C. Coddet, Mater Design (1980-2015) 54 (2014) 727–733, doi:10.1016/j.matdes.2013.08.085.
[39] P. Jiang, C. Blawert, M.L. Zheludkevich, Corros Mater Degradation 1 (1) (2020) 92–158, doi:10.3390/cmd1010007.
[40] H. Okamoto, J\ Phase Equilibria 15 (1) (1994) 129–130, doi:10.1007/BF02667700.
[41] S. Cai, T. Lei, N. Li, F. Feng, Mater Sci Engineering: C 32 (8) (2012) 2570–2577, doi:10.1016/j.msec.2012.07.042.

[42] A.F. Lotfabadi, M.H. Idris, A. Ourdjini, M.R. Abdul Kadir, S. Farahany, H.R. Bakhsheshi-Rad, Bullet Mater Sci 36 (6) (2013) 1103–1113, doi:10.1007/s12034-013-0566-9.

[43] M. Asadollahi, E. Gerashi, R. Alizadeh, R. Mahmudi, J Mater Res Technol 21 (2022) 4473–4489, doi:10.1016/j.jmrt.2022.11.041.

[44] Q. Peng, X. Li, N. Ma, R. Liu, H. Zhang, J Mech Behav Biomed Mater 10 (2012) 128–137, doi:10.1016/j.jmbbm.2012.02.024.

[45] J. Chen, et al., Metals (Basel) 6 (11) (Oct. 2016) 259, doi:10.3390/met6110259.

[46] E. Zhang, D. Yin, L. Xu, L. Yang, K. Yang, Mater Sci Engineer: C 29 (3) (2009) 987–993, doi:10.1016/j.msec.2008.08.024.

[47] Y.C. Lee, A.K. Dahle, D.H. StJohn, Metallurg Mater Trans A 31 (11) (2000) 2895–2906, doi:10.1007/BF02830349.

[48] S. Keerti, A. Gokhale, J. Jain, E.-W. Huang, Tribol Lett 65 (4) (2017) 140, doi:10.1007/s11249-017-0925-6.

[49] M. Němec, V. Gärtnerová, M. Klementová, A. Jäger, Mater Charact 106 (2015) 428–436, doi:10.1016/j.matchar.2015.05.038.

[50] Y. Lu, A.R. Bradshaw, Y.L. Chiu, I.P. Jones, J Alloys Compd 614 (2014) 345–352, doi:10.1016/j.jallcom.2014.06.078.

[51] X. Liu, D. SHAN, Y. SONG, E. HAN, Trans Nonferrous Metals Soc China 20 (7) (2010) 1345–1350, doi:10.1016/S1003-6326(09)60302-2.

[52] Y. Song, E.-H. Han, D. Shan, C.D. Yim, B.S. You, Corros Sci 60 (2012) 238–245, doi:10.1016/j.corsci.2012.03.030.

[53] H.R. Bakhsheshi-Rad, et al., Mater Corrosion 65 (10) (2014) 999–1006, doi:10.1002/maco.201307492.

[54] M. Masoumi, M. Pekguleryuz, Mater Sci Engineering: A 529 (2011) 207–214, doi:10.1016/j.msea.2011.09.019.

[55] S. Nayak, B. Bhushan, R. Jayaganthan, P. Gopinath, R.D. Agarwal, D. Lahiri, J Mech Behav Biomed Mater 59 (2016) 57–70, doi:10.1016/j.jmbbm.2015.12.010.

[56] Z. Zou, J. Chen, H. Yan, B. Su, X. Gong, J Mater Eng Perform 25 (5) (2016) 1974–1985, doi:10.1007/s11665-016-2041-4.

[57] S. Zhang, et al., Acta Biomater 6 (2) (2010) 626–640, doi:10.1016/j.actbio.2009.06.028.

[58] C. Zhao, et al., J Mater Sci Technol 35 (1) (2019) 142–150, doi:10.1016/j.jmst.2018.09.015.

[59] H.-Y. Ha, J.-Y. Kang, J. Yang, C.D. Yim, B.S. You, Corros Sci 75 (2013) 426–433, doi:10.1016/j.corsci.2013.06.027.

[60] Y. Song, E.-H. Han, D. Shan, C.D. Yim, B.S. You, Corros Sci 65 (2012) 322–330, doi:10.1016/j.corsci.2012.08.037.

[61] Y. Yan, et al., J Alloys Compd 693 (2017) 1277–1289, doi:10.1016/j.jallcom.2016.10.017.

[62] M. Němec, A. Jäger, K. Tesař, V. Gärtnerová, Mater Charact 134 (2017) 69–75, doi:10.1016/j.matchar.2017.10.017.

[63] M. Němec, V. Gärtnerová, A. Jäger, Mater Charact 119 (2016) 129–136, doi:10.1016/j.matchar.2016.07.016.

[64] M. Němec, V. Gärtnerová, in: European Microscopy Congress2016: Proceedings, Wiley, 2016, pp. 241–242, doi:10.1002/9783527808465.EMC2016.5004.

[65] F. Long, G. Chen, M. Zhou, Q. Shi, Q. Liu, J Magn Alloys 11 (6) (2023) 1931–1943, doi:10.1016/j.jma.2021.08.029.

[66] E. Koç, M.E. Turan, Mater Res Express 6 (8) (2019) 0865b5, doi:10.1088/2053-1591/ab1955.

[67] E. Koç, M.B. Kannan, M. Ünal, E. Candan, J Alloys Compd 648 (2015) 291–296, doi:10.1016/j.jallcom.2015.06.227.

[68] D.N. Pham, S. Hiromoto, M. O, E. Kobayashi, Surf Coat Technol 421 (2021) 127414, doi:10.1016/j.surfcoat.2021.127414.

[69] A.R. Setiawan, A.A. Putera Satria, A. Basuki, U.A. Wibowo, IOP Conf Ser Mater Sci Eng 553 (1) (2019) 012005, doi:10.1088/1757-899X/553/1/012005.

[70] P. Liu, H. Jiang, Z. Cai, Q. Kang, Y. Zhang, J Magn Alloys 4 (3) (2016) 188–196, doi:10.1016/j.jma.2016.07.001.

[71] Z. Zareian, M. Emamy, M. Malekan, H. Mirzadeh, W.J. Kim, A. Bahmani, Mater Sci Engineer: A 774 (2020) 138929, doi:10.1016/j.msea.2020.138929.

[72] Y. Zheng, Y. Li, J. Chen, Z. Zou, Corros Sci 90 (2015) 445–450, doi:10.1016/j.corsci.2014.10.043.

[73] M. Cheng, et al., J Alloys Compd 691 (2017) 95–102, doi:10.1016/j.jallcom.2016.08.164.

[74] Z.R. Zeng, M.Z. Bian, S.W. Xu, C.H.J. Davies, N. Birbilis, J.F. Nie, Mater Sci Engineer: A 674 (2016) 459–471, doi:10.1016/j.msea.2016.07.049.

[75] X. Qian, et al., Mater Des 224 (2022) 111322, doi:10.1016/j.matdes.2022.111322.

[76] M. Zohrevand, M. Mohammadi-Zerankeshi, F. Nobakht-Farin, R. Alizadeh, R. Mahmudi, J Mater Res Technol 20 (2022) 1204–1215, doi:10.1016/j.jmrt.2022.07.072.

[77] K. Yan, et al., J Magn Alloys 7 (2) (2019) 305–314, doi:10.1016/j.jma.2019.02.006.

[78] K. Yan, et al., Mater Sci Engineering: A 739 (2019) 513–518, doi:10.1016/j.msea.2018.09.007.

[79] X. Luo, S. Yang, M. Li, Z. Tang, S. Wang, B. Huang, Trans Indian Instit Metals 74 (12) (2021) 3063–3073, doi:10.1007/s12666-021-02373-9.

[80] D. YIN, E. ZHANG, S. ZENG, Trans Nonferrous Metals Soc China 18 (4) (2008) 763–768, doi:10.1016/S1003-6326(08)60131-4.

[81] M. Saini, World J Clin Cases 3 (1) (2015) 52, doi:10.12998/wjcc.v3.i1.52.

[82] B.P. Zhang, Y. Wang, L. Geng, Biomaterials - Physics and Chemistry, InTech, 2011, doi:10.5772/23929.

[83] C.J. Boehlert, K. Knittel, Mater Sci Engineering: A 417 (1–2) (2006) 315–321, doi:10.1016/j.msea.2005.11.006.

[84] S. Ramesh, G. Anne, H.S. Nayaka, S. Sahu, M.R. Ramesh, J Mater Eng Perform 28 (4) (2019) 2053–2062, doi:10.1007/s11665-019-04007-0.

[85] M. Kavyani, G.R. Ebrahimi, M. Sanjari, M. Haghshenas, J Magn Alloys 4 (2) (2016) 89–98, doi:10.1016/j.jma.2016.05.002.

[86] Q. Li, G.J. Huang, X.D. Huang, S.W. Pan, C.L. Tan, Q. Liu, J Magn Alloys 5 (2) (2017) 166–172, doi:10.1016/j.jma.2017.06.001.

[87] N. Stanford, M.R. Barnett, in: Magnesium Technology 2012, John Wiley & Sons, Inc., Hoboken, NJ, USA, 2012, pp. 207–211, doi:10.1002/9781118359228.ch39.

[88] X. Gu, Y. Zheng, Y. Cheng, S. Zhong, T. Xi, Biomaterials 30 (4) (2009) 484–498, doi:10.1016/j.biomaterials.2008.10.021.

[89] H. Jia, X. Feng, Y. Yang, J Magn Alloys 3 (3) (2015) 247–252, doi:10.1016/j.jma.2015.08.006.

[90] M. Sabbaghian, R. Mahmudi, K.S. Shin, Mater Sci Engineering: A 792 (2020) 139828, doi:10.1016/j.msea.2020.139828.

[91] G. Anne et al., 2019, pp. 339–343. doi: 10.1007/978-3-030-05789-3_50.

[92] N. El Mahallawy, A. Ahmed Diaa, M. Akdesir, H. Palkowski, Materwiss Werksttech 47 (1) (2016) 37–46, doi:10.1002/mawe.201500468.

[93] D.B. Prabhu, S. Dhamotharan, G. Sathishkumar, P. Gopalakrishnan, K.R. Ravi, Mater Sci Engineering: A 730 (2018) 223–231, doi:10.1016/j.msea.2018.06.002.

[94] H. Somekawa, A. Singh, T. Mukai, Scr Mater 60 (6) (2009) 411–414, doi:10.1016/j.scriptamat.2008.11.017.

[95] C. Shuai, S. Li, S. Peng, P. Feng, Y. Lai, C. Gao, Mater Chem Front 3 (4) (2019) 544–562, doi:10.1039/c8qm00507a.

[96] G. Song, A. Atrens, Adv Eng Mater 5 (12) (2003) 837–858, doi:10.1002/adem.200310405.

[97] F. Witte, et al., Biomaterials 26 (17) (2005) 3557–3563, doi:10.1016/j.biomaterials.2004.09.049.

[98] J.H. Nordlien, S. Ono, N. Masuko, K. Nisancioglu, Corros Sci 39 (8) (1997) 1397–1414, doi:10.1016/S0010-938X(97)00037-1.

[99] R. Udhayan, D.P. Bhatt, J Power Sources 63 (1) (1996) 103–107, doi:10.1016/S0378-7753(96)02456-1.

[100] K. Aramaki, Corros Sci 43 (8) (2001) 1573–1588, doi:10.1016/S0010-938X(00)00144-X.

[101] D. Persaud-Sharma, A. McGoron, J Biomim Biomater Tissue Eng 12 (2012) 25–39, doi:10.4028/www.scientific.net/JBBTE.12.25.

[102] D.R. Lide (Ed.), CRC Handbook of Chemistry and Physics, CRC press, Boca Raton, 2005.

[103] Y. Xin, K. Huo, H. Tao, G. Tang, P.K. Chu, Acta Biomater 4 (6) (2008) 2008–2015, doi:10.1016/j.actbio.2008.05.014.

[104] A. Yamamoto, S. Hiromoto, Mater Sci Engineering: C 29 (5) (2009) 1559–1568, doi:10.1016/j.msec.2008.12.015.

[105] M.K.I. Kanai, Kanai's Manual of Clinical Laboratory Medicine, 31st ed., Kinbara-shuppan, Tokyo, 1998.

[106] Y. Xin, T. Hu, P.K. Chu, Acta Biomater 7 (4) (2011) 1452–1459, doi:10.1016/j.actbio.2010.12.004.

[107] D. Mei, S.V. Lamaka, X. Lu, M.L. Zheludkevich, Corros Sci 171 (2020) 108722, doi:10.1016/j.corsci.2020.108722.

[108] T. Kokubo, H. Takadama, Biomaterials 27 (15) (2006) 2907–2915, doi:10.1016/j.biomaterials.2006.01.017.

[109] I. Marco, F. Feyerabend, R. Willumeit-Römer, O. Van der Biest, in: TMS2015 Supplemental Proceedings, Wiley, 2015, pp. 497–506, doi:10.1002/9781119093466.ch63.

[110] L. Wei, Z. Gao, RSC Adv 13 (12) (2023) 8427–8463, doi:10.1039/D2RA07829E.

[111] D.F. Williams, R.L. Williams, in: B.D. Ratner, A.S. Hoffman, F.J. Schoen, J.E. Lemons (Eds.), Biomaterials Science An Introduction to Materials in Medicine, 2nd ed., Elsevier, 2004, pp. 430–439. ch. 6.

[112] A.C. Hänzi, I. Gerber, M. Schinhammer, J.F. Löffler, P.J. Uggowitzer, Acta Biomater 6 (5) (2010) 1824–1833, doi:10.1016/j.actbio.2009.10.008.

[113] N.I. Zainal Abidin, et al., Corros Sci 75 (2013) 354–366, doi:10.1016/j.corsci.2013.06.019.

[114] J.H. Hanks, R.E. Wallace, Exp Biol Med 71 (2) (1949) 196–200, doi:10.3181/00379727-71-17131.

[115] N.I. Zainal Abidin, A.D. Atrens, D. Martin, A. Atrens, Corros Sci 53 (11) (2011) 3542–3556, doi:10.1016/j.corsci.2011.06.030.

[116] N.T. Kirkland, et al., J Mater Sci Mater Med 23 (2) (2012) 283–291, doi:10.1007/s10856-011-4517-y.

[117] X.B. Chen, et al., Acta Biomater 10 (3) (2014) 1463–1474, doi:10.1016/j.actbio.2013.11.016.

[118] N.T. Kirkland, J. Lespagnol, N. Birbilis, M.P. Staiger, Corros Sci 52 (2) (2010) 287–291, doi:10.1016/j.corsci.2009.09.033.

[119] I. Marco, et al., Eur Cell Mater 33 (2017) 90–104, doi:10.22203/eCM.v033a07.

[120] F. Feyerabend, et al., J Mater Sci Mater Med 23 (1) (2012) 9–24, doi:10.1007/s10856-011-4490-5.

[121] S. Zhang, et al., Mater Sci Engineering: C 29 (6) (2009) 1907–1912, doi:10.1016/j.msec.2009.03.001.

[122] J.-W. Chang, P.-H. Fu, X.-W. Guo, L.-M. Peng, W.-J. Ding, Corros Sci 49 (6) (2007) 2612–2627, doi:10.1016/j.corsci.2006.12.011.

[123] H.R. Bakhsheshi-Rad, et al., Mater Corros 65 (12) (2014) 1178–1187, doi:10.1002/maco.201307588.

[124] Y. Song, D. Shan, E.-H. Han, Mater Sci Engineering: C 33 (1) (2013) 78–84, doi:10.1016/j.msec.2012.08.008.

[125] S. Zhang, J. Li, Y. Song, C. Zhao, C. Xie, X. Zhang, Adv Eng Mater 12 (5) (2010), doi:10.1002/adem.200980052.

[126] F. Cao, K. Deng, K. Nie, J. Kang, H. Niu, J Alloys Compd 770 (2019) 1208–1220, doi:10.1016/j.jallcom.2018.08.191.

[127] R. Udhayan, D.P. Bhatt, J Power Sources 63 (1) (1996) 103–107, doi:10.1016/S0378-7753(96)02456-1.

[128] D.B. Prabhu, P. Gopalakrishnan, K.R. Ravi, J Alloys Compd 812 (2020) 152146, doi:10.1016/j.jallcom.2019.152146.

[129] S. Zhang, et al., Mater Sci Engineering: C 68 (2016) 414–422, doi:10.1016/j.msec.2016.06.017.

[130] M.E. Moussa, H.I. Mohamed, M.A. Waly, G.S. Al-Ganainy, A.B. Ahmed, M.S. Talaat, J Alloys Compd 792 (2019) 1239–1247, doi:10.1016/j.jallcom.2019.03.363.

[131] J. Dong, et al., J Magn Alloys 10 (9) (2022) 2491–2509, doi:10.1016/j.jma.2021.11.018.

[132] Z.-Z. Yin, et al., J Magn Alloys 8 (1) (2020) 42–65, doi:10.1016/j.jma.2019.09.008.

[133] M.N. Sarian, et al., Bioact Mater 12 (2022) 42–63, doi:10.1016/j.bioactmat.2021.10.034.

[134] Y. Song, S. Zhang, J. Li, C. Zhao, X. Zhang, Acta Biomater 6 (5) (2010) 1736–1742, doi:10.1016/j.actbio.2009.12.020.

[135] S.-X. Zhang, J.-N. Li, Y. Song, C.-L. Zhao, X.-N. Zhang, Front Mater Sci China 4 (2) (2010,) 116–119, doi:10.1007/s11706-010-0026-z.

[136] S. Singh, et al., JOM 67 (4) (2015) 702–712, doi:10.1007/s11837-015-1364-1.

[137] J. Li, et al., Bioinorg Chem Appl 2011 (2011) 1–7, doi:10.1155/2011/192671.

[138] D.N. Pham, S. Hiromoto, T. Yamazaki, M. O, E. Kobayashi, ACS Appl Bio Mater 4 (9) (2021) 6881–6892, doi:10.1021/acsabm.1c00594.

[139] S. Yang, et al., Trans Indian Instit Metals 76 (8) (2023) 2273–2283, doi:10.1007/s12666-023-02928-y.

[140] I. Kozina, H. Krawiec, M. Starowicz, M. Kawalec, Int J Mol Sci 22 (15) (2021) 8301, doi:10.3390/ijms22158301.

[141] I.M. Ghayad, M.A. Maamoun, W.A. Metwally, Z.M. El-Baradie, A.N. Abdel-Azim, J Mater Eng Perform 25 (10) (2016) 4171–4180, doi:10.1007/s11665-016-2258-2.

[142] N.S. Goud, in: A Comprehensive Guide to Toxicology in Nonclinical Drug Development, Elsevier, 2017, pp. 825–840, doi:10.1016/B978-0-12-803620-4.00031-1.

[143] S. Capuani, G. Malgir, C.Y.X. Chua, A. Grattoni, Bioeng Transl Med 7 (3) (2022), doi:10.1002/btm2.10300.

[144] J. Li, et al., Biomaterials 31 (22) (2010) 5782–5788, doi:10.1016/j.biomaterials.2010.04.023.

[145] S. Yoshizawa, A. Brown, A. Barchowsky, C. Sfeir, Acta Biomater 10 (6) (2014) 2834–2842, doi:10.1016/j.actbio.2014.02.002.

[146] X. Wang, A. Ito, Y. Sogo, X. Li, A. Oyane, Acta Biomater 6 (3) (2010) 962–968, doi:10.1016/j.actbio.2009.08.038.

[147] W. Yu, et al., RSC Adv 6 (51) (2016) 45219–45230, doi:10.1039/C6RA03998G.

[148] Y. He, Int J Mol Med (2011), doi:10.3892/ijmm.2011.707.

[149] J. Li, et al., Mater Sci Engineering: B 176 (20) (2011) 1785–1788, doi:10.1016/j.mseb.2011.05.029.

[150] E. Zhang, X. Zhao, J. Hu, R. Wang, S. Fu, G. Qin, Bioact Mater 6 (8) (2021) 2569–2612, doi:10.1016/j.bioactmat.2021.01.030.

[151] A. Nostro, et al., APMIS 120 (9) (2012) 733–742, doi:10.1111/j.1600-0463.2012.02900.x.

[152] H. Qin, et al., Biomaterials 53 (2015) 211–220, doi:10.1016/j.biomaterials.2015.02.096.

[153] H. Hu, W. Zhang, Y. Qiao, X. Jiang, X. Liu, C. Ding, Acta Biomater 8 (2) (2012) 904–915, doi:10.1016/j.actbio.2011.09.031.

[154] T.-N. Phan, T. Buckner, J. Sheng, J.D. Baldeck, R.E. Marquis, Oral Microbiol Immunol 19 (1) (2004) 31–38, doi:10.1046/j.0902-0055.2003.00109.x.

[155] C. Pan, R. Xu, J. Chen, Q. Zhang, L. Deng, Q. Hong, Int J Biol Macromol 271 (2024) 132487, doi:10.1016/j.ijbiomac.2024.132487.

[156] M.B. Gorbet, M.V. Sefton, Biomaterials 25 (26) (2004) 5681–5703, doi:10.1016/j.biomaterials.2004.01.023.

[157] J. Gao, L. Qiao, L. Li, Y. Wang, Trans Nonferrous Metals Soc China 16 (3) (2006) 539–544, doi:10.1016/S1003-6326(06)60094-0.

[158] J. Chen, et al., Prog Org Coat 186 (2024) 108058, doi:10.1016/j.porgcoat.2023.108058.

[159] Y. Zhang, et al., Nat Med 22 (10) (2016) 1160–1169, doi:10.1038/nm.4162.

[160] C. Pan, et al., Int J Biol Macromol 279 (2024) 135166, doi:10.1016/j.ijbiomac.2024.135166.

[161] Y. He, et al., Sci Bull (Beijing) 54 (3) (2009) 484–491, doi:10.1007/s11434-009-0080-z.

[162] J. Yan, et al., J Mater Sci Mater Med 24 (6) (2013) 1515–1525, doi:10.1007/s10856-013-4906-5.

[163] Y. Chen, et al., Mater Sci Engineering: C 42 (2014) 116–123, doi:10.1016/j.msec.2014.05.014.